Article

Improved green and red GRAB sensors for monitoring spatiotemporal serotonin release in vivo

🔴 Check for updates

Fei Deng ®[1,2,3,8], **Jinxia Wan** ®[1,2,8], **Guochuan Li**[1,2], **Hui Dong** ®[1,2], **Xiju Xia**[1,2,4], **Yipan Wang**[1,2], **Xuelin Li**[1,2], **Chaowei Zhuang**[5], **Yu Zheng** ®[1,2,6], **Laixin Liu**[1,2,6], **Yuqi Yan**[1,2,6], **Jiesi Feng**[1,2], **Yulin Zhao** ®[1,2], **Hao Xie** ®[5] & **Yulong Li** ®[1,2,4,6,7]✉

The serotonergic system plays important roles in both physiological and pathological processes, and is a therapeutic target for many psychiatric disorders. Although several genetically encoded GFP-based serotonin (5-HT) sensors were recently developed, their sensitivities and spectral profiles are relatively limited. To overcome these limitations, we optimized green fluorescent G-protein-coupled receptor (GPCR)-activation-based 5-HT (GRAB$_{5-HT}$) sensors and developed a red fluorescent GRAB$_{5-HT}$ sensor. These sensors exhibit excellent cell surface trafficking and high specificity, sensitivity and spatiotemporal resolution, making them suitable for monitoring 5-HT dynamics in vivo. Besides recording subcortical 5-HT release in freely moving mice, we observed both uniform and gradient 5-HT release in the mouse dorsal cortex with mesoscopic imaging. Finally, we performed dual-color imaging and observed seizure-induced waves of 5-HT release throughout the cortex following calcium and endocannabinoid waves. In summary, these 5-HT sensors can offer valuable insights regarding the serotonergic system in both health and disease.

Serotonin (5-HT) is an important monoamine signaling molecule that is present virtually throughout the body, regulating a wealth of biological processes[1]. In the central nervous system (CNS), 5-HT is an intensively studied neuromodulator involved in a wide range of neurobiological processes, such as emotion, learning and memory, reward, appetite and sleep–wake cycles[1–3]. Moreover, impaired 5-HT transmission is associated with a broad range of CNS disorders, including anxiety, addiction, depression and epilepsy[4–6]. As a consequence, many psychotropic and psychedelic drugs have been developed to target the serotonergic system[7]. Therefore, understanding the serotonergic transmission in both physiological and pathological processes requires the ability to

directly monitor 5-HT dynamics in behaving animals in real time, which requires sensitive detection tools. Although classic detection methods such as microdialysis and fast-scan cyclic voltammetry provide valuable accesses for measuring 5-HT levels, they lack the high spatiotemporal resolution, specificity and sensitivity and minimal invasiveness needed for the in vivo detection of 5-HT[8–10].

Recent advances in genetically encoded fluorescent 5-HT sensors have led to tools that surpass classic methods; however, these sensors have not yet hit the proverbial 'sweet spot' with respect to balancing apparent affinity with the magnitude of the response. Specifically, sensors based on GPCRs, including GRAB$_{5-HT1.0}$, PsychLight2

[1]State Key Laboratory of Membrane Biology, School of Life Sciences, Peking University, Beijing, China. [2]PKU-IDG/McGovern Institute for Brain Research, Beijing, China. [3]Institute of Molecular Physiology, Shenzhen Bay Laboratory, Shenzhen, China. [4]Peking University–Tsinghua University–National Institute of Biological Sciences Joint Graduate Program, Academy for Advanced Interdisciplinary Studies, Peking University, Beijing, China. [5]Department of Automation, Tsinghua University, Beijing, China. [6]Peking-Tsinghua Center for Life Sciences, New Cornerstone Science Laboratory, Academy for Advanced Interdisciplinary Studies, Peking University, Beijing, China. [7]Chinese Institute for Brain Research, Beijing, China. [8]These authors contributed equally: Fei Deng, Jinxia Wan. ✉e-mail: yulongli@pku.edu.cn

and sDarken[11–13], have high affinity for 5-HT but produce only a modest change in fluorescence. The periplasmic-binding-protein-based sensor iSeroSnFR[14] has a large response but low affinity to 5-HT. Thus, monitoring 5-HT dynamics in vivo requires a more sensitive sensor that has a high affinity and sufficiently large response.

In the CNS, the serotonergic system interacts with other neurotransmitters and neuromodulators[15]; thus, simultaneously imaging 5-HT and other neurochemicals can provide valuable information about the regulation of cognitive functions controlled by these signaling processes. Unfortunately, most existing sensors for neurochemicals contain green fluorescent protein (GFP) as the fluorescent module, as do all genetically encoded 5-HT sensors, precluding combined imaging owing to spectral overlap. Although a near-infrared 5-HT nanosensor based on single-wall carbon nanotubes has been reported[16], it might not be suitable for use in living animals owing to limited sensitivity. However, red-shifted sensors, such as a previously reported red calcium sensor[17], are compatible with other green fluorescent sensors and blue-light-excitable actuators, with intrinsically superior optical properties—including deeper tissue penetration, reduced autofluorescence and low phototoxicity—owing to their longer excitation wavelengths. Thus, red-shifted 5-HT sensors suitable for in vivo imaging, particularly multiplexed imaging, are needed.

Here, we report a series of green and red fluorescent 5-HT sensors based on the 5-HTR4 subtype. The green fluorescent sensor, gGRAB$_{5-HT3.0}$ (g5-HT3.0), produces an ~1,300% fluorescence increase in response to 5-HT, making it superior to existing green fluorescent 5-HT sensors both in vitro and in vivo. The red-shifted sensor, rGRAB$_{5-HT1.0}$ (r5-HT1.0), produces a >300% fluorescence increase to 5-HT in vitro and is suitable for multicolor imaging in vivo. Moreover, using mesoscopic imaging, we have revealed distinct patterns of 5-HT release under different conditions.

Results

Development and optimization of GRAB$_{5-HT}$ sensors

To expand the dynamic range and spectral profile of GRAB$_{5-HT}$ sensors, we first systematically searched for the most suitable GPCR scaffold by transplanting the third intracellular loop (ICL3) from existing green and red fluorescent GRAB sensors into a wide range of 5-HT receptor subtypes (Fig. 1a). For green fluorescent sensors, we used ICL3 derived from green GRAB$_{5-HT1.0}$ (g5-HT1.0) or GRAB$_{NE1m}$[18] as the donor (including circularly permuted enhanced GFP (cpEGFP) and surrounding linkers). Possibly owing to the conserved structures among the class A family of GPCRs, we obtained candidate sensors that yielded a >50% increase in fluorescence ($\Delta F/F_0$) in response to 10 μM 5-HT following the screening of replacement sites. g5-HT1.1, a green fluorescent candidate based on 5-HTR4, had a higher response than did the original g5-HT1.0 sensor. To develop red fluorescent 5-HT sensors, we transplanted the ICL3 derived from rGRAB$_{DA1m}$[19] into the 5-HTR2C, 5-HTR4 and 5-HTR6 scaffolds—we chose these three subtypes on the basis of their high performance when

developing the green fluorescent 5-HT sensors. The top candidate, r5-HT0.1, was based on the 5-HTR4 subtype, with an ~40% $\Delta F/F_0$ (Fig. 1a).

To improve the sensors' sensitivity, we optimized g5-HT1.1 and r5-HT0.1 by performing saturation mutagenesis of critical residues thought to affect structural coupling, fluorescence intensity[20], protein folding[21] or conformational change[22].

We performed further iterative optimization by screening more than 4,500 candidates, which yielded 2 intermediate green fluorescent sensors, g5-HT2h and g5-HT2m, and the final sensor, g5-HT3.0 (Fig. 1b,c and Supplementary Fig. 1a–c). When expressed in HEK293T cells, these green fluorescent 5-HT sensors showed good trafficking to the cell surface and a robust fluorescence increase in response to 100 μM 5-HT (Fig. 1c,d and Extended Data Fig. 1a–c). Notably, g5-HT3.0 ($\Delta F/F_0$, ~1,300%) showed a much larger response than did g5-HT1.0, Psych-Light2 or iSeroSnFR. Moreover, g5-HT3.0 is much brighter than the other 5-HT sensors and has a higher signal-to-noise ratio (SNR) (Fig. 1d). Dose–response curves showed that g5-HT3.0 produces a larger $\Delta F/F_0$ than do previous sensors over a wide range of concentrations, with an half-maximum effective concentration (EC$_{50}$) of ~150 nM (Fig. 1e). We also generated a 5-HT-insensitive version of g5-HT3.0, g5-HT3.0mut, by introducing the p.D131[3.32]F (superscript 3.32 defined by the Ballesteros–Weinstein numbering system) substitution[22,23]; we confirmed that g5-HT3.0mut localizes to the plasma membrane but does not respond to 5-HT, even at 100 μM (Fig. 1b–e and Supplementary Fig. 1a,c).

Similarly, we generated a red fluorescent 5-HT sensor called r5-HT1.0 by screening >3,000 candidates and introducing the p.D131[3.32]Q and p.D149[3.50]H substitutions into a 5-HT-insensitive version, r5-HTmut (Fig. 1b–e and Supplementary Fig. 1d,f). Both r5-HT1.0 and r5-HTmut localized to the plasma membrane when expressed in cultured HEK293T cells (Fig. 1c). Application of 10 μM 5-HT to cells expressing r5-HT1.0 elicited an ~330% increase in fluorescence, but had no effect on cells expressing r5-HTmut (Fig. 1c,d). The EC$_{50}$ of r5-HT1.0 was ~790 nM (Fig. 1e). Moreover, unlike the cpmApple-based calcium sensor jRGECO1a—in which blue light causes an increase in fluorescence[17]—r5-HT1.0 did not show obvious photoactivation (Fig. 1f), suggesting that it is compatible with blue-light-excitable optogenetic opsins and green fluorescent sensors, although it did exhibit a small off response when exposed to intense blue-light illumination of up to 10 mW (Extended Data Fig. 1k,l).

### Characterization of GRAB$_{5-HT}$ sensors

Next, we expressed these 5-HT sensors in HEK293T cells and characterized their pharmacology, specificity, spectra and kinetics. We found that both g5-HT3.0 and r5-HT1.0 inherited the pharmacological specificity of the parent 5-HTR4 receptor; their 5-HT induced responses were blocked by the 5-HTR4-specific antagonist RS 23597-190 (RS), but not the 5-HTR2C-specific antagonist SB 242084 (SB). Both sensors were unaffected by a wide range of signaling molecules, including the 5-HT precursor, 5-HT metabolite and a variety of other neurotransmitters

Fig. 1 | Development of improved green fluorescent 5-HT sensors and red 5-HT sensors. a, Top, the strategy for developing GRAB$_{5-HT}$ sensors. Bottom, performance of sensor candidates based on different receptor subtypes for green (left) and red 5-HT sensors (right). The dashed horizontal line represents g5-HT1.0 response (bottom left), and the best candidate green and red sensors are denoted by enlarged green and red dots, respectively. **b**, Top, optimization of the replacement site, linker, cpFP and GPCR. Bottom, various candidates' responses to 5-HT (10 μM). **c**, Representative images of sensor expression (top, with 5-HT) and response to 5-HT (bottom) in HEK293T cells. Insets with white dashed outlines in images have either enhanced contrast (top) or different pseudocolor scales (bottom); 100 μM 5-HT was used for green sensors, and 10 μM 5-HT was used for red sensors. Similar results were observed for more than 50 cells. Scale bars, 20 μm. **d**, Brightness (left), peak $\Delta F/F_0$ (middle) and SNR (right) of different 5-HT sensors. The SNR of each sensor was relative to that of g5-HT1.0. arb.u., arbitrary units. The basal brightness of g5-HT1.0 was set to 1. $n = 119/3$ (119 cells from 3 coverslips) for g5-HT3.0, 82/3 for g5-HT1.0, 64/3 for PsychLight2, 139/3

for iSeroSnFR, 92/3 for g5-H3.0mut, 159/5 for r5-HT1.0 and 191/5 for r5-HTmut; 100 μM 5-HT was used for green sensors; 10 μM 5-HT was used for red sensors. For statistical analysis, a one-way analysis of variance (ANOVA) followed by Tukey's multiple-comparison tests was used for green sensors; for peak $\Delta F/F_0$, $F_{4,491} = 387.1$, $P = 2.76 \times 10^{-150}$, post hoc test: $P = 0$, 4.15×10^{-9}, 0 and 0 for g5-HT3.0 versus other sensors (g5-HT1.0, PsychLight2, iSeroSnFR and g5-HT3.0mut, respectively); for relative SNR, $F_{4,491} = 285.7$, $P = 1.13 \times 10^{-126}$, post hoc test: $P = 5.62 \times 10^{-7}$, 2.22×10^{-8}, 7.33×10^{-8} and 4×10^{-9} for g5-HT3.0 versus other sensors. Two-tailed Student's t-test for r5-HT1.0 and r5-HTmut; for peak $\Delta F/F_0$, $P = 3.13 \times 10^{-72}$; for relative SNR, $P = 2.67 \times 10^{-43}$. **e**, Dose–response curves of different 5-HT sensors. $n = 3$ wells for each sensor, with 300–500 cells per well. **f**, Schematic of the photoactivation properties of jRGECO1a and r5-HT1.0 (left), representative traces (middle) and peak $\Delta F/F_0$ (right) in response to blue light (488 nm, without imaging) in cells expressing jRGECO1a or r5-HT1.0. $n = 105/4$ for jRGECO1a and 88/4 for r5-HT1.0. Two-tailed Student's t-test, $P = 2.07 \times 10^{-48}$. Data are shown as mean ± s.e.m. in **d**–**f**, with the error bars or shaded regions indicating the s.e.m. ***$P < 0.001$.

and neuromodulators (Fig. 2a and Extended Data Fig. 2a,b). The emission spectra of the green fluorescent (with a peak at 520 nm) and red fluorescent (with a peak at 595 nm) sensors are well-separated, and one-/two-photon excitation peaks for g5-HT3.0 and r5-HT1.0 are at 505/920 nm and 560/1050 nm, respectively (Fig. 2b and Extended Data Fig. 1d,e). The isosbestic point for g5-HT3.0 under one-photon excitation is 425 nm. We measured the on rate (τ_{on}) by locally puffing 10 μM of 5-HT on the cells, and the off rate (τ_{off}) by puffing the 5-HTR4 antagonist RS in the continued presence of 10 μM 5-HT (Fig. 2c,d), revealing sub-second τ_{on} rates and faster τ_{off} rates than those of our previously reported g5-HT1.0 sensor[11]. Mean τ_{off} rates were 1.66 s, 1.90 s, 0.38 s and 0.51 s for g5-HT3.0, g5-HT2h, g5-HT2m and r5-HT1.0, respectively (Fig. 2e and Extended Data Fig. 1f).

We then expressed the g5-HT3.0 and r5-HT1.0 sensors in cultured rat cortical neurons, and found that they trafficked well to the cell membrane. Application of a saturating concentration of 5-HT induced fluorescence increases of ~2,700% for g5-HT3.0 and ~400% for r5-HT1.0, but had no effect on neurons expressing g5-HT3.0mut or r5-HTmut (Fig. 2f,g,i,j). In cultured cortical neurons, EC_{50} values for g5-HT3.0, g5-HT2h, g5-HT2m and r5-HT1.0 were 80 nM, 70 nM, 2.4 μM and 600 nM, respectively (Fig. 2h,k and Extended Data Fig. 1g), and they exhibited high specificity to 5-HT (Extended Data Fig. 2c–f). g5-HT3.0 was brighter and had a greater fluorescence change and higher SNR in cultured neurons (Extended Data Fig. 3) than did previously reported GFP-based 5-HT sensors.

d
g5-HT3.0 g5-HT1.0 PsychLight2 iSeroSnFR g5-HT3.0mut r5-HT1.0 r5-HTmut
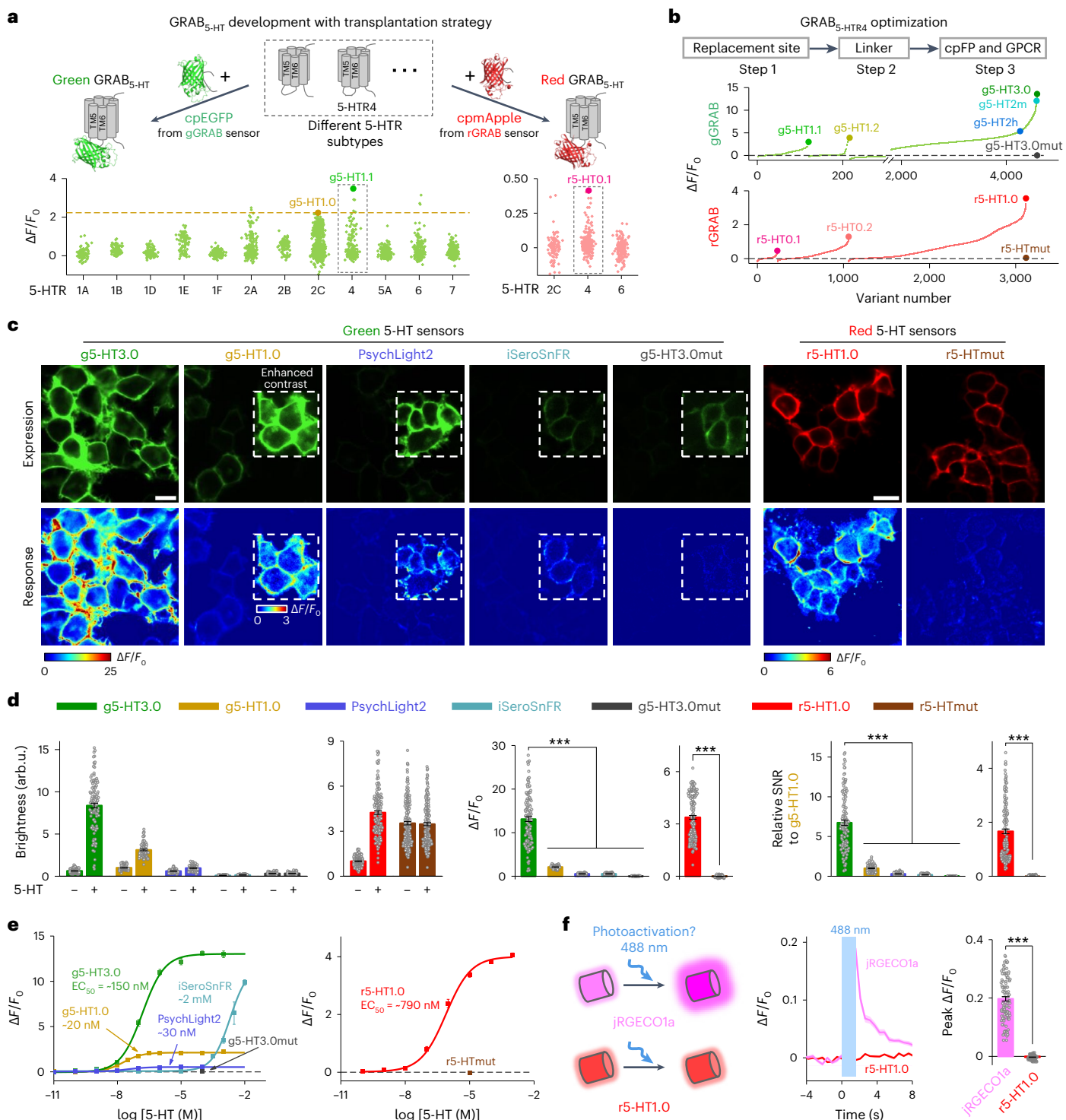
To investigate whether our 5-HT sensors are coupled to downstream signaling pathways, we used the luciferase complementation assay[24] and the Tango assay[25] to measure the GPCR-mediated G_s and β-arrestin pathways, respectively. These sensors showed negligible downstream coupling; by contrast, the wild-type 5-HTR4 receptor had high basal activity and robust dose-dependent coupling (Fig. 2l and Extended Data Fig. 1h,i). In addition, our sensors did not undergo β-arrestin-mediated internalization or desensitization when expressed in cultured neurons; the 5-HT-elicited increase in fluorescence was stable for up to 2 h in the continuous presence of 10 μM 5-HT (Fig. 2m and Extended Data Fig. 1j). Furthermore, expression of these sensors showed minimal buffering effects in vitro and did not have an obvious impact on 5-HT-related behaviors (Extended Data Fig. 4). This suggests that these sensors are well-suited for monitoring serotonin dynamics without affecting normal cell physiology or animal behaviors.

Using the sensitive g5-HT3.0 sensor and a red dopamine (DA) sensor, rGRAB$_{DA3m}$ (rDA3m)[26], we performed dual-color confocal imaging in the mouse dorsal raphe nucleus (DRN) to simultaneously monitor the 5-HT and DA dynamics with high spatiotemporal resolution. Unlike the synchronous releases elicited by electrical stimulation, the spontaneous transients are separated, with a higher frequency of 5-HT events than of DA events (Extended Data Fig. 5). Notably, g5-HT3.0 demonstrated remarkable sensitivity in detecting spontaneous release events with a diameter as small as ~10 μm, reflecting its potential to detect single-cell, or even sub-cellular, 5-HT release at the micrometer scale.

Measuring endogenous 5-HT release in freely moving mice

To determine whether our red fluorescent sensor can monitor endogenous 5-HT dynamics in vivo, we expressed either r5-HT1.0 or r5-HTmut in the basal forebrain (BF) and channelrhodopsin-2 (ChR2)[27] in serotonergic neurons in the DRN of SERT-cre mice[28] (Fig. 3a). Optical stimulation of the DRN induced time-locked transient increases in r5-HT1.0 fluorescence, the amplitude of which increased progressively with increasing duration of stimulation; moreover, the selective serotonin transporter (SERT) inhibitor fluoxetine further increased the response amplitude and prolonged the decay time of the response (Fig. 3b–e). As expected, no response was measured for the 5-HT-insensitive r5-HTmut sensor (Fig. 3b–e).

To leverage the red-shifted 5-HT sensor's spectrum in conjunction with green fluorescent sensors, we expressed either r5-HT1.0 or r5-HTmut in the BF and the axon-targeted green fluorescent calcium sensor axon-GCaMP6s[29] in DRN serotonergic neurons, which project to the BF and regulate sleep–wake cycles[11,30], of SERT-cre mice. We then performed dual-color fiber-photometry recording in the BF while recording electroencephalography (EEG) and electromyography (EMG) signals to track the sleep–wake state in the animals (Fig. 3f). We found that both the r5-HT1.0 and GCaMP6s signals were higher during the wake state and non-rapid eye movement (NREM) sleep than during rapid eye movement (REM) sleep (Fig. 3g,j). Additionally, r5-HT1.0 revealed oscillations in 5-HT levels (Fig. 3h). Moreover, the r5-HT1.0 and GCaMP6s signals were temporally correlated with no detectable lag, revealing the rapid release of 5-HT and high consistency between 5-HT release and the increase in presynaptic calcium (Fig. 3i). By contrast, the r5-HTmut signal was largely unchanged throughout sleep–wake cycles (Fig. 3j and Extended Data Fig. 6).

To compare the performance of our optimized g5-HT3.0 sensor with that of previously reported 5-HT sensors, we performed bilateral recordings in the BF during sleep–wake cycles in mice expressing g5-HT3.0 in one hemisphere and g5-HT1.0, PsychLight2 or iSeroSnFR in the other (Extended Data Fig. 7a,d,g). We found that the SNR during the wake state and NREM sleep was larger for the g5-HT3.0 sensor than for the other three sensors, and the the g5-HT3.0 sensor measured more-robust oscillations during NREM sleep (Extended Data Fig. 7b,c,e,f,h,i). Moreover, g5-HT3.0 exhibited greater sensitivity than did g5-HT1.0 and iSeroSnFR in detecting modest 5-HT changes, such as in the basal amygdala (BA) of the water-restricted mice during delivery of 5% glucose (Extended Data Fig. 8).

Additionally, we observed that sensors in mice injected with higher-titer virus in the BF exhibited a larger SNR during sleep–wake cycles than did those in mice injected with lower-titer virus, underscoring the importance of selecting an appropriate virus titer (Supplementary Fig. 2).

**Mesoscopic imaging of cortical 5-HT dynamics in mice**

Although 5-HT has crucial roles in the cerebral cortex, its serotonergic projections are notably sparser in this region than are those in subcortical regions, such as the BF[31]. Therefore, measuring 5-HT release in the cortex requires a highly sensitive 5-HT sensor. We expressed the

Fig. 2 | Characterization of 5-HT sensors in HEK293T cells and cultured rat cortical neurons. a, Normalized $\Delta F/F_0$ of g5-HT3.0 and r5-HT1.0 in response to different compounds (each at 10 μM, except RS at 100 μM). 5-HTP, 5-hydroxytryptophan; 5-HIAA, 5-hydroxyindole acetic acid; DA, dopamine; NE, norepinephrine; HA, histamine; MT, melatonin; OA, octopamine; Glu, glutamate; GABA, γ-aminobutyric acid; ACh, acetylcholine; Gly, glycine. Norm., normalized. $n = 3$ wells per group, 200–500 cells per well. One-way ANOVA followed by Tukey's multiple-comparison test, for g5-HT3.0, $F_{13,28} = 745.7$, $P = 5.74 \times 10^{-32}$, post hoc test: $P = 0$ for 5-HT versus 5-HT+RS and other compounds; for r5-HT1.0, $F_{13,28} = 180.6$, $P = 2.02 \times 10^{-23}$, post hoc test: $P = 0$ for 5-HT versus 5-HT+RS and other compounds. **b**, One-photon excitation (Ex) and emission (Em) spectra and two-photon excitation spectra of g5-HT3.0 and r5-HT1.0 in the absence (dashed line) or presence of 10 μM 5-HT (solid line). F.I., fluorescence intensity. **c**, Kinetic analysis of the g5-HT3.0 sensor. Illustration of the local puffing system (left), representative traces of sensor fluorescence increase in response to puffing of 5-HT (top right) and decrease in response to RS (bottom right). **d**, Kinetic analysis of the r5-HT1.0 sensor, similar to **c**. **e**, On and off kinetics for the sensors. $n = 10/3$ (10 cells from 3 coverslips) for g5-HT3.0 on kinetics, 12/4 for g5-HT3.0 off kinetics, 9/3 for r5-HT1.0 on kinetics and 12/4 for r5-HT1.0 off kinetics. **f**, Representative images showing the expression of g5-HT3.0 and g5-HT3.0mut and their response to 100 μM 5-HT in cultured rat cortical neurons. The inset in the g5-HT3.0mut response image shows the contrast-enhanced expression image. **g**, Representative traces and peak response summary of g5-HT3.0 and g5-HT3.0mut in response to 100 μM 5-HT. $n = 96/5$ (96 regions of interest (ROIs) from 5 coverslips) for g5-HT3.0 and 92/5 for g5-HT3.0mut. Two-tailed Student's t-test, $P = 1.40 \times 10^{-53}$ for g5-HT3.0 versus g5-HT3.0mut. **h**, The dose–response curve of g5-HT3.0. $n = 76/4$. **i**, Representative images showing the expression and responses of r5-HT1.0 and r5-HTmut to 10 μM 5-HT. **j**, Representative traces and peak response summary of r5-HT1.0 and r5-HTmut in response to 10 μM 5-HT. $n = 80/4$ for r5-HT1.0 and 60/3 for r5-HTmut. Two-tailed Student's t-test, $P = 4.46 \times 10^{-70}$ for r5-HT1.0 versus r5-HTmut. **k**, The dose–response curve of r5-HT1.0. $n = 80/4$. **l**, Downstream coupling tests. WT, wild type; Ctrl, control, without expression of WT 5-HTR4 or sensors. $n = 3$ wells per group, 200–500 cells per well. One-way ANOVA followed by Tukey's multiple-comparison tests, for the luciferase complementation assay, $F_{3,8} = 256$, $P = 2.77 \times 10^{-8}$, post hoc test: $P = 0$ and 0.37 for g5-HT3.0 versus 5-HTR4 (WT) and Ctrl in 1 mM 5-HT, respectively, $P = 0$ and 1 for r5-HT1.0 versus 5-HTR4 (WT) and Ctrl, respectively; for the Tango assay, $F_{3,8} = 766.4$, $P = 3.55 \times 10^{-10}$, post hoc test: $P = 0$ and 0.89 for g5-HT3.0 versus 5-HTR4 (WT) and Ctrl in 100 μM 5-HT, respectively, $P = 0$ and 0.86 for r5-HT1.0 versus 5-HTR4 (WT) and Ctrl, respectively. **m**, Normalized $\Delta F/F_0$ of g5-HT3.0 and r5-HT1.0 in response to the 2-h application of 10 μM 5-HT, followed by 100 μM RS. $n = 3$ wells for each sensor. One-way repeated measures ANOVA followed by Tukey's multiple-comparison tests, for g5-HT3.0, $F = 359.8$, $P = 0.034$, post hoc test: $P = 1.29 \times 10^{-6}$ for baseline versus 0 h, $P = 1.76 \times 10^{-6}$ for 2.0 h versus RS, $P = 1$, 0.77, 1 and 1 for 0 h versus 0.5 h, 1.0 h, 1.5 h and 2.0 h, respectively; for r5-HT1.0, $F = 250.9$, $P = 0.04$, post hoc test: $P = 2.85 \times 10^{-6}$ for baseline versus 0 h, $P = 5.82 \times 10^{-6}$ for 2.0 h versus RS, $P = 0.95$, 0.44, 0.66 and 0.64 for 0 h versus 0.5 h, 1 h, 1.5 h and 2.0 h, respectively. HEK293T cells were used in **a–e** and **l**; rat cortical neurons were used in **f–k** and **m**. All scale bars, 20 μm. Data are shown as mean ± s.e.m. in **a**, **e**, **g**, **h** and **j–m**, with the error bars or shaded regions indicating the s.e.m. ***$P < 0.001$, NS, not significant.

g5-HT3.0 sensor in neurons throughout the whole brain by injecting adeno-associated viruses into the transverse sinus of neonatal (postnatal day 0 (P0)–P1) mice[32]. We then measured g5-HT3.0 fluorescence throughout the whole dorsal cortex using mesoscopic imaging[33] in response to optogenetic stimulation of DRN serotonergic neurons expressing ChrimsonR[34] (Fig. 4a). We found that light pulses induced

transient increases in g5-HT3.0 fluorescence, with increasing stimulation frequency causing increasingly larger responses (Fig. 4b,c). As a negative control, no response was measured when we expressed a membrane-tethered EGFP (memEGFP) (Fig. 4b,c and Extended Data Fig. 9g). Notably, we found that treating mice with the SERT blocker fluoxetine caused a gradual increase in baseline 5-HT levels and slowed
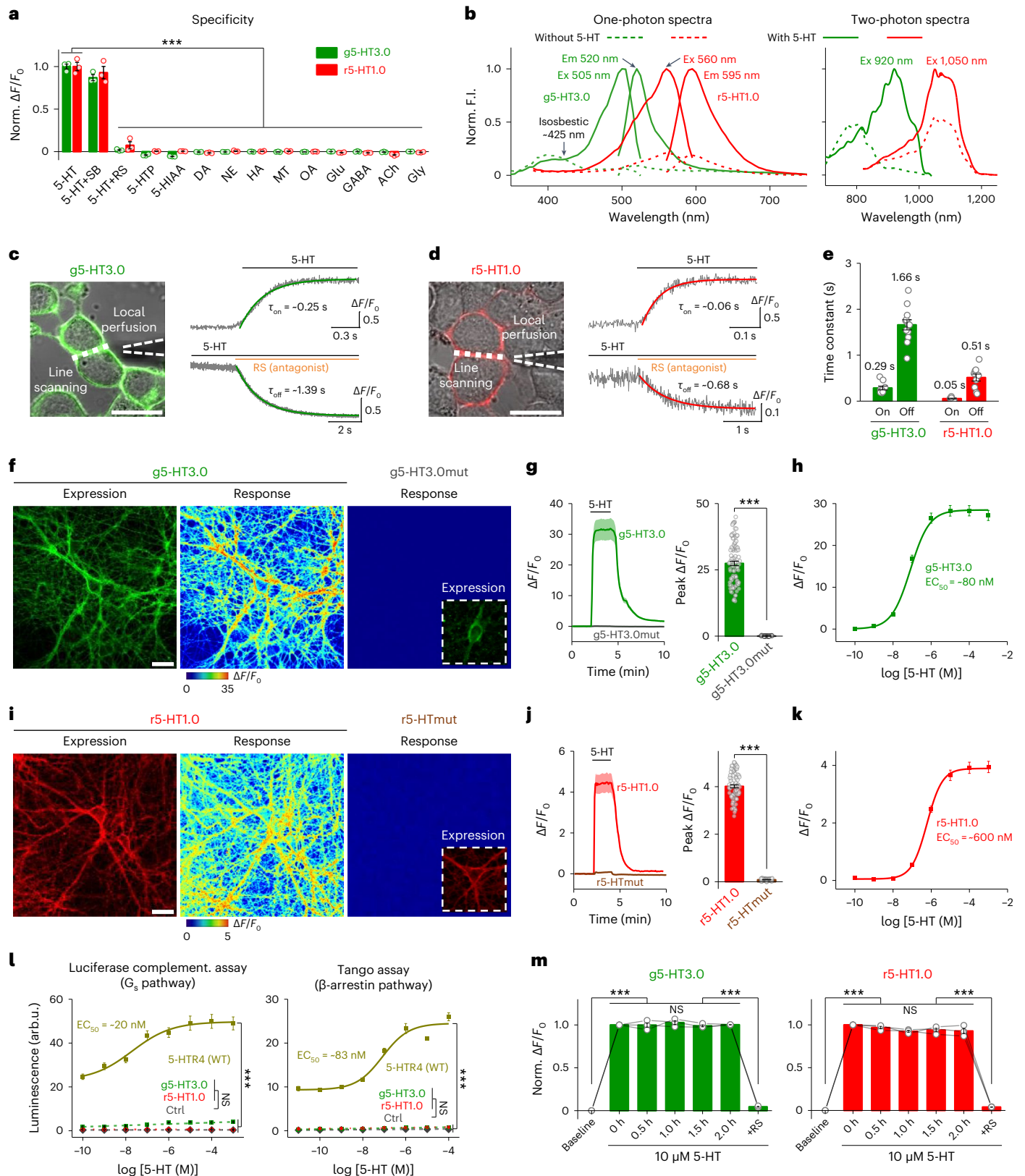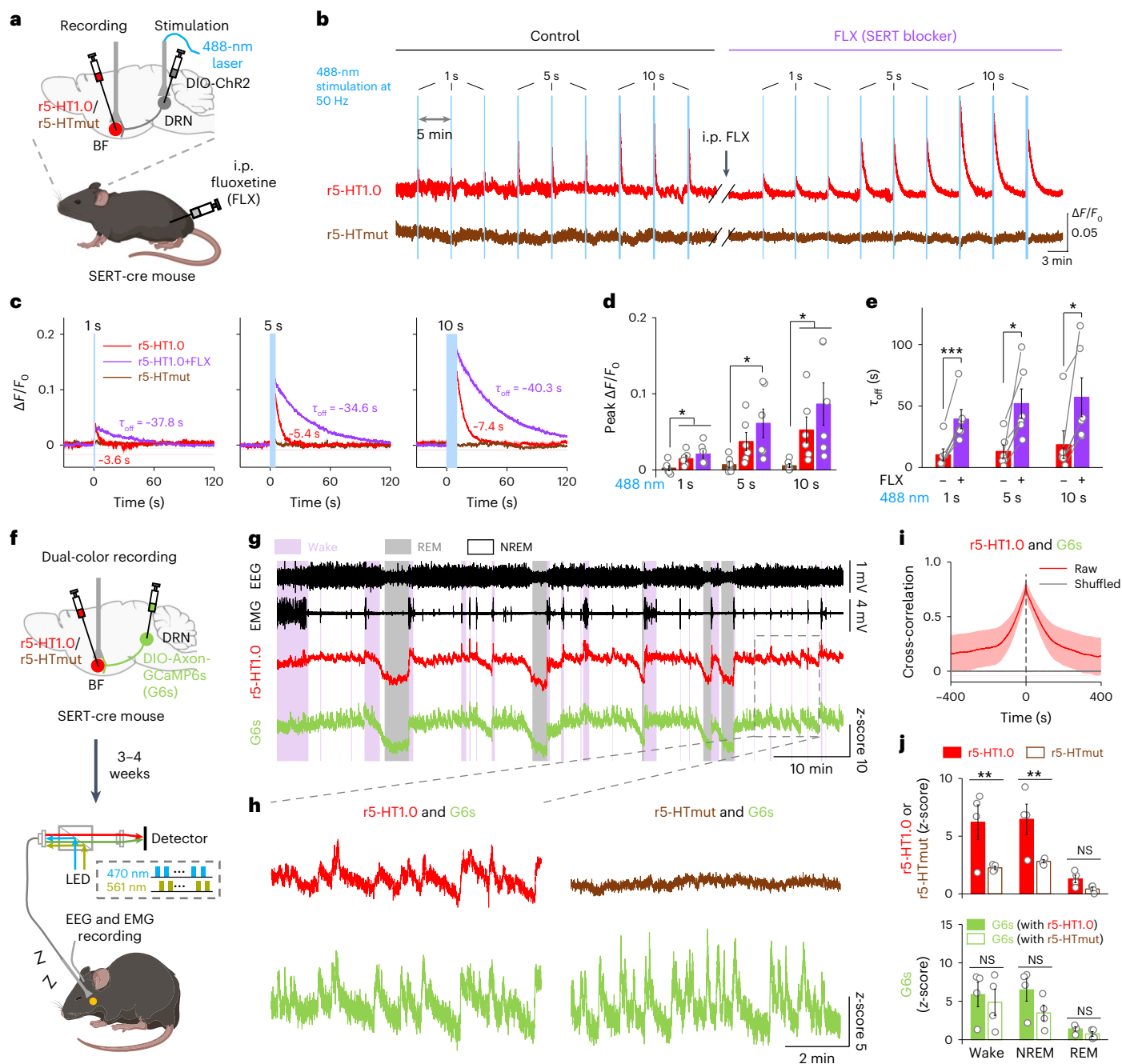
Fig. 3 | The red GRAB$_{5-HT}$ sensor can monitor endogenous 5-HT release in freely moving mice. a, The fiber-photometry recording setup involving red 5-HT sensors, with optogenetic activation of DRN in SERT-cre mice. i.p., intraperitoneal. **b**, Representative $\Delta F/F_0$ traces of r5-HT1.0 and r5-HTmut in response to optical stimulation in the DRN under different stimulation durations before or after fluoxetine (FLX) application. **c**, Average $\Delta F/F_0$ traces of r5-HT1.0 and r5-HTmut under different stimulation durations in an example mouse. Blue shading, period of 488-nm stimulation. **d**, Peak responses of r5-HT1.0 and r5-HTmut under different durations of stimulation. $n = 6$ mice for each treatment. Two-tailed Student's t-tests, for r5-HTmut versus r5-HT1.0, $P = 0.030$, 0.052 and 0.041 under 1-s, 5-s and 10-s stimulation, respectively; for r5-HTmut versus r5-HT1.0+FLX, $P = 0.016$, 0.034 and 0.033 under 1-s, 5-s and 10-s stimulation, respectively. **e**, Decay kinetics of r5-HT1.0 with or without FLX application under different durations of stimulation. $n = 6$ mice for each treatment. Two-tailed paired t-tests for r5-HT1.0 and r5-HT1.0+FLX, $P = 4.44 \times 10^{-4}$, 1.44×10^{-2},

3.19×10^{-2} for 1-s, 5-s and 10-s stimulation, respectively. **f**, The setup for dual-color recording of r5-HT1.0 or r5-HTmut and GCaMP6s (G6s) during sleep–wake cycles. **g**, Representative traces of simultaneous EEG, EMG, r5-HT1.0 and G6s recording during sleep–wake cycles in freely behaving mice. Pink shading, wake state; gray shading, REM sleep. **h**, Zoom-in traces of r5-HT1.0 and G6s (from **g**) or r5-HTmut and G6s (mainly during NREM sleep). **i**, The average cross-correlation between r5-HT1.0 and G6s signals during sleep–wake cycles. **j**, Average responses of 5-HT sensors (red channel, r5-HT1.0 or r5-HTmut) and G6s (green channel). $n = 4$ mice for each group. Two-way repeated measures ANOVA, followed by Tukey's multiple-comparison tests; for r5-HT1.0 versus r5-HTmut, post hoc test: $P = 5.65 \times 10^{-3}$, 9.22×10^{-3} and 0.47 during wake, NREM and REM sleep state, respectively; for G6s (with r5-HT1.0) versus G6s (with r5-HTmut), post hoc test: $P = 0.56$, 0.11 and 0.71 during wake, NREM and REM sleep state, respectively. Data are shown as mean ± s.e.m. in **c**–**e**, **i** and **j**, with the error bars or shaded regions indicating the s.e.m. *$P < 0.05$, **$P < 0.01$, ***$P < 0.001$, NS, not significant.
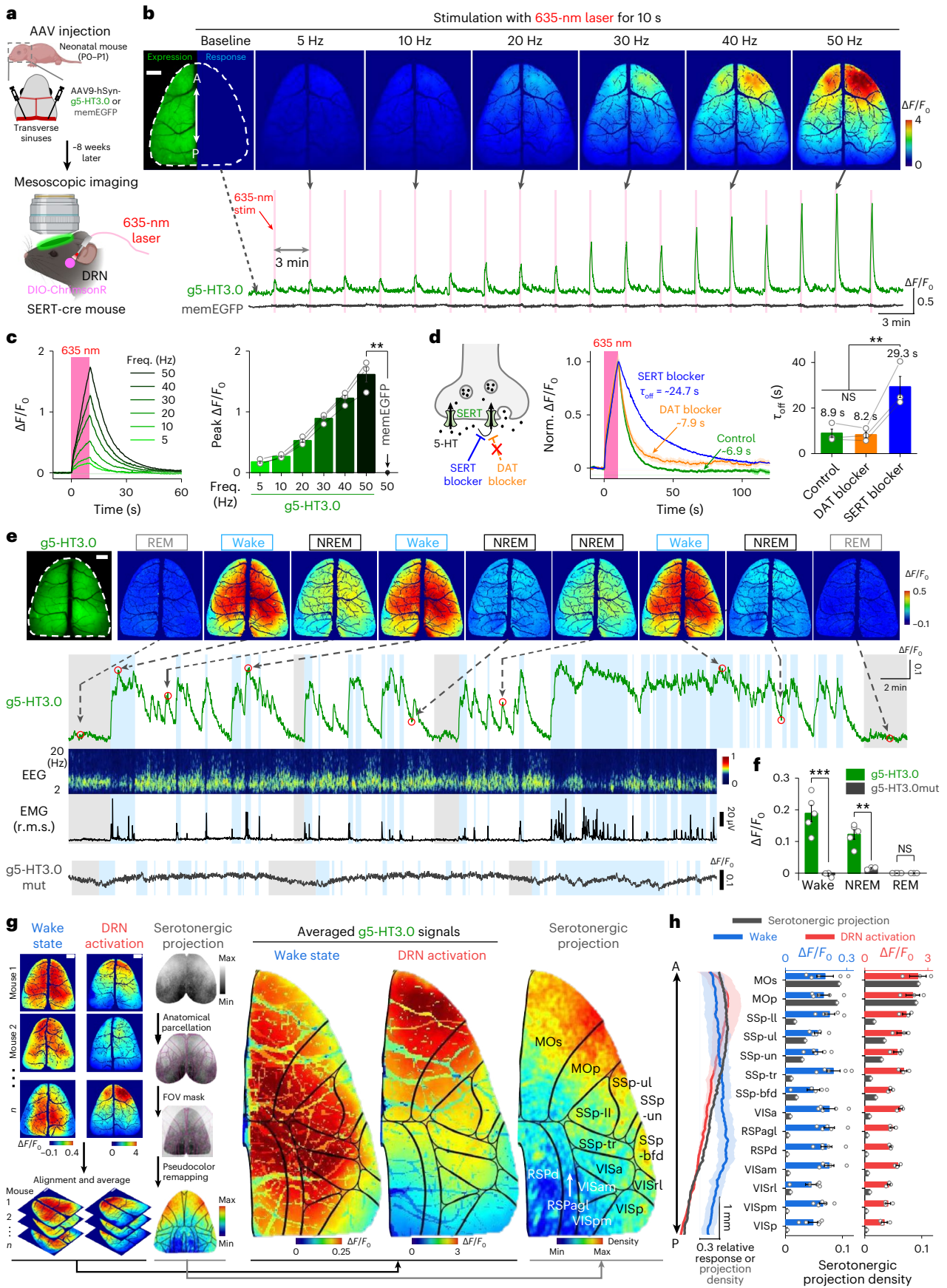
the decay rate of stimulation-induced transients; by contrast, the dopamine transporter (DAT) blocker GBR-12909 had no effect (Fig. 4d and Extended Data Fig. 9a–f).

We then used g5-HT3.0 to measure physiological 5-HT dynamics during sleep–wake cycles using mesoscopic imaging combined with simultaneous EEG and EMG recordings. Similar to our results measured

Fig. 4 | Mesoscopic imaging of mouse dorsal cortex shows that GRAB₅-HT3.0 reveals 5-HT release in vivo. a, Setup of mesoscopic imaging experiments. **b**, Top, representative images showing the cortical g5-HT3.0 expression and response to optical stimulation in the DRN with incremental frequencies. Bottom, representative traces of g5-HT3.0 and a negative control memEGFP. The dashed white outline encloses the ROI. **c**, Representative $\Delta F/F_0$ traces of g5-HT3.0 (left) and peak $\Delta F/F_0$ (right) with increased frequencies of the 635-nm laser. $n = 3$ mice for each group. Two-tailed Student's t-tests, $P = 8.48 \times 10^{-3}$ for g5-HT3.0 versus memEGFP under 50-Hz stimulation. **d**, The effect of an SERT blocker and DAT blocker on the extracellular 5-HT level (left). Representative $\Delta F/F_0$ traces of g5-HT3.0 (middle) and decay kinetics (right) during 10 s of 50-Hz stimulation after treatment with the indicated compounds. One-way repeated measures ANOVA followed by Tukey's multiple-comparison test, $F = 28.9$, $P = 4.18 \times 10^{-3}$, post hoc test: $P = 0.98$ for DAT blocker versus control, 6.45×10^{-3} for SERT blocker versus control and 5.72×10^{-3} for SERT blocker versus DAT blocker. **e**, Top, representative fluorescence and pseudocolor images of g5-HT3.0 during sleep–wake cycles. Bottom, representative traces of g5-HT3.0 response, EEG, EMG (by root mean square, r.m.s.) and g5-HT3.0mut response in the dorsal cortex during sleep–wake cycles. The dashed white outline in the top left image encloses the ROI. Dashed arrows and red circles indicate the timepoint of frames shown at the top. Gray shading, REM sleep; light blue shading, wake state. **f**, g5-HT3.0 and g5-HT3.0mut responses in mice during the awake state and during NREM and REM sleep. $n = 5$ mice for g5-HT3.0 and 3 mice for g5-HT3.0mut. Two-way repeated measures ANOVA followed by Tukey's multiple-comparison tests for g5-HT3.0 and g5-HT3.0mut, $P = 5.77 \times 10^{-6}$, 1.89×10^{-3} and 1 during the wake, NREM and REM sleep state, respectively. **g**, Left, snapshots of g5-HT3.0 responses in different mice in the awake state and DRN activation in the mice, and a serotonergic projection map modified from the Allen Mouse Brain CCF. Middle, average pseudocolor images of g5-HT3.0 responses under the indicated conditions. Right, serotonergic projection map overlaid with black outlines aligned to the Allen Brain (right). MOs, secondary motor area; MOp, primary motor area; SSp-ll, primary somatosensory area, lower limb; SSp-ul, primary somatosensory area, upper limb; SSp-un, primary somatosensory area, unassigned; SSp-tr, primary somatosensory area, trunk; SSp-bfd, primary somatosensory area, barrel field; VISa, anterior area; VISam, anteromedial visual area; VISrl, rostrolateral visual area; VISpm, posteromedial visual area; VISp, primary visual area; RSPagl, retrosplenial area, lateral agranular part; RSPd, retrosplenial area, dorsal part. $n = 5$ and 3 mice for the awake state and DRN activation group, respectively. **h**, Average relative responses of g5-HT3.0 and serotonergic projection density along the anterior-to-posterior (AP) axis (left) and summary of g5-HT3.0 signals or serotonergic projection density in different cortex regions. $n = 5$ and 3 mice for the awake state and DRN activation group, respectively. All scale bars, 1 mm. Data are shown as mean ± s.e.m. in **c**, **d**, **f** and **h**, with the error bars or shaded regions indicating the s.e.m. **$P < 0.01$, ***$P < 0.001$, NS, not significant.

in the subcortical BF (Extended Data Fig. 7), the g5-HT3.0 signal in the dorsal cortex was highest during the awake state, followed by the NREM and REM states, with oscillations during NREM sleep. Moreover, using g5-HT3.0mut, we found no change in fluorescence in sleep–wake cycles (Fig. 4e,f).

We further segmented the dorsal cortex into various brain regions on the basis of the Allen Common Coordinate Framework v3 (CCFv3) atlas[35] and analyzed the spatial distribution of the 5-HT signals during optogenetic stimulation and sleep–wake cycles. We found that the 5-HT signals measured in different brain regions were relatively spatially homogeneous and temporally synchronized during sleep–wake cycles (Fig. 4g and Extended Data Fig. 9h), reminiscent of our previous results recorded in subcortical regions[11]. By contrast, when we optogenetically stimulated DRN serotonergic neurons, the 5-HT signals had a graded pattern, decreasing along the anterior-to-posterior axis (Fig. 4g,h); this pattern was consistent with the anatomically heterogeneous density of serotonergic projections throughout the cortex[31].

These results demonstrate that our next-generation g5-HT3.0 sensor is sufficiently sensitive to monitor 5-HT release in vivo, with high spatiotemporal resolution.

Dual-color imaging of neurochemical waves during seizure

The serotonergic system has been suggested to protect the CNS from epileptiform activity[36–39], which is characterized by excessive and hypersynchronous neuronal firing. However, little is known about the spatiotemporal dynamics of 5-HT release during and after seizure, let alone about the relationship between 5-HT and other seizure-related signals such as calcium and endocannabinoid (eCB). Therefore, we used a strategy similar to that depicted in Fig. 4a to pan-neuronally co-express g5-HT3.0 together with jRGECO1a or r5-HT1.0 together with eCB2.0 (ref. 40) throughout the whole brain. We then performed dual-color mesoscopic imaging to measure 5-HT and calcium or eCB dynamics in the mouse dorsal cortex while performing EEG recording to identify seizures induced by an injection of the glutamate receptor agonist kainic acid[41] (Fig. 5a). Similar to previous reports[40,42], we observed an increase in Ca²⁺ signals during the kainic-acid-induced seizure, followed by a spreading wave of Ca²⁺ with a larger magnitude. In the same mouse, we observed a spreading wave of 5-HT, reported by g5-HT3.0 signals, that closely followed the Ca²⁺ wave (Fig. 5b,f and Supplementary Video 1). The waves reported by g5-HT3.0 and jRGECO1a originated in approximately the same location and propagated with similar speed (at ~76 μm s⁻¹ and ~83 μm s⁻¹, respectively) and in the same direction, primarily from the lateral cortex to the medial region (Fig. 5g,h). As a negative control, seizure activity had no effect on the signal measured using g5-HT3.0mut (Fig. 5c,f and Extended Data Fig. 10a,b).

Finally, we obtained similar results in mice co-expressing r5-HT1.0 and eCB2.0, with a propagating wave of 5-HT release following the eCB wave. Moreover, the waves reported by r5-HT1.0 and eCB2.0 originated in approximately the same location, propagated at similar speeds (~83 μm s⁻¹ and ~81 μm s⁻¹, respectively) and in the same direction (Fig. 5d,f–h and Supplementary Video 2). As described above, seizure activity had no effect on the signal measured using r5-HTmut (Fig. 5e,f and Extended Data Fig. 10c,d).

Taken together, these results demonstrate that our g5-HT3.0 and r5-HT1.0 sensors can reliably report 5-HT release in vivo with high

Fig. 5 | Dual-color imaging of cortex-wide neurochemical waves during seizures. a, Setup of dual-color mesoscopic imaging in a kainic acid (KA)-induced seizure model. sCMOS, scientific complementary metal oxide semiconductor camera. **b**, Representative images and $\Delta F/F_0$ traces of g5-HT3.0 and jRGECO1a during seizures. Two ROIs (500 μm in diameter) are labeled; ROI 1 (the white circle) and ROI 2 (the white dashed circle) show the maximum response regions of g5-HT3.0 and jRGECO1a, respectively. The solid and dashed lines in traces correspond to ROI 1 and ROI 2, respectively. The red shading in the EEG trace indicates the epileptic discharges. **c**, Representative $\Delta F/F_0$ traces of g5-HT3.0mut and jRGECO1a during seizures, similar to **b**. Images are also shown in Extended Data Fig. 10b. **d**, Representative images and $\Delta F/F_0$ traces of r5-HT1.0 and eCB2.0 during seizures, similar to **b** except that ROI 1 (the white circle) and ROI 2 (the white dashed circle) show the maximum response regions of r5-HT1.0 and eCB2.0, respectively. **e**, Representative traces of r5-HTmut and eCB2.0 signals during seizures, similar to **d**. Images are also shown in Extended Data Fig. 10d. **f**, Peak responses of the sensors. $n = 5$ mice for the group co-expressing g5-HT3.0 and jRGECO1a, $n = 4$ for g5-HT3.0mut and jRGECO1a, $n = 3$ for r5-HT1.0 and eCB2.0, $n = 3$ for r5-HTmut and eCB2.0. Two-tailed Student's t-tests, $P = 2.36 \times 10^{-4}$ for g5-HT3.0 versus g5-HT3.0mut, $P = 0.64$ for jRGECO1a between the two groups; $P = 4.41 \times 10^{-3}$ for r5-HT1.0 versus r5-HTmut, $P = 0.45$ for eCB2.0 between the two groups. **g**, Representative images of the wave propagation detected by the indicated sensors. The red circle indicates the origin of waves; small white arrows indicate the wave-propagating velocity vector; green arrows indicate example propagating trajectories. L, lateral, M, medial, A, anterior, P, posterior. **h**, Probability distributions of wave-propagating speed and direction calculated using indicated sensors. All scale bars, 1 mm. Data are shown as mean ± s.e.m. in **f** and **h**, with the error bars indicating the s.e.m. **$P < 0.01$, ***$P < 0.001$, NS, not significant.

sensitivity, specificity and spatiotemporal resolution both under physiological conditions and during seizure activity.

Discussion

Here, we report the development, optimization, characterization and in vivo application of a series of genetically encoded red and green fluorescent 5-HT sensors. Particularly, the dual-color imaging revealed that the seizure-induced 5-HT waves were spatially correlated—but

lagged behind—Ca^{2+} and eCB waves, consistent with the idea that serotonergic activity may protect against neuronal hyperactivity[36,38]. The temporal lag between calcium and 5-HT signals indicates the possible neuromodulation of 5-HT release within serotonergic axons following the hyperactivity of cortical neurons, but the precise mechanism underlying this delay is yet to be determined.

Our next-generation green fluorescent GRAB$_{5-HT}$ sensors have three advantages over previously reported genetically encoded fluorescent
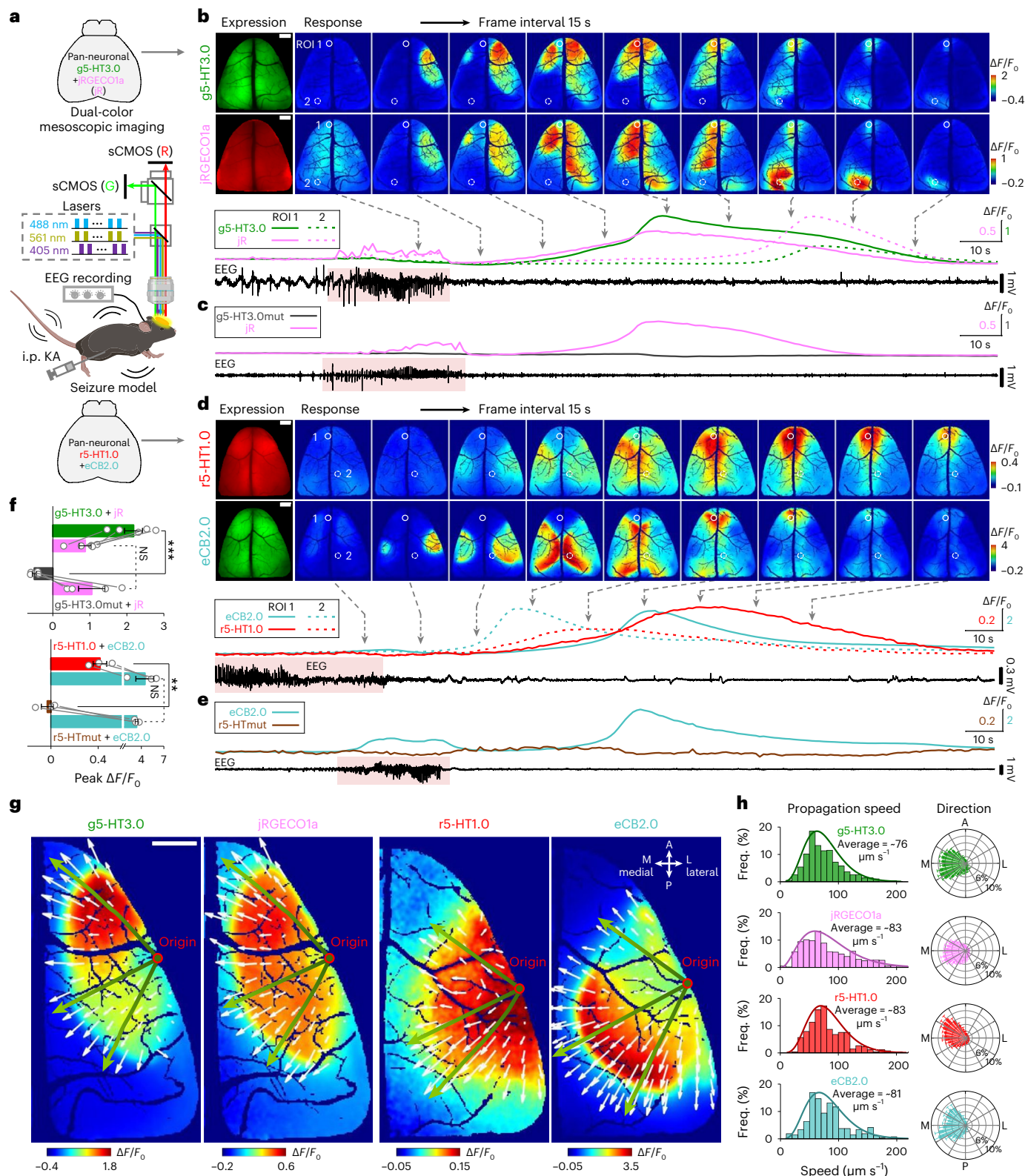
5-HT sensors. First, g5-HT3.0 is more sensitive, owing to its large response, high affinity and brightness, making it more suitable for both in vitro and in vivo applications. Second, these sensors—g5-HT3.0 and g5-HT2m—span a range of affinities, from hundred-nanomoles to micromoles, effectively bridging the critical gap in measuring intermediate concentrations of 5-HT. Specifically, the g5-HT3.0 sensor is generally suitable for detecting 5-HT dynamics across a wide range of scenarios, from modest 5-HT release (for example, reward) to large changes in 5-HT levels (for example, seizure). However, in scenarios in which the 5-HT concentration is notably high, such as in the gut, g5-HT2m may offer a more appropriate detection range. Thus, users can now access a toolbox, including previous sensors such as g5-HT1.0 and iSeroSnFR, covering a wide range of physiological and pathological 5-HT concentrations[43–45]. Third, these sensors have rapid kinetics and are suitable for tracking transient 5-HT release in real time. When rapid dynamics are required, g5-HT2m is particularly suitable because its sub-second off kinetics are faster than those of g5-HT3.0 and g5-HT2h.

Our red fluorescent 5-HT sensor expands the spectral profile of genetically encoded 5-HT sensors and is suitable for dual-color imaging. We simultaneously recorded signals of r5-HT1.0 and axon-targeted GCaMP6s in the mouse BF during sleep–wake cycles and found that the two signals were closely correlated, consistent with Ca^{2+}-dependent, rapid 5-HT release. Because r5-HT1.0 lacks an isosbestic point, to fully leverage the advantages of multiplex imaging with r5-HT1.0 and most green sensors, users can consider employing another spectral-compatible fluorescent protein, such as TagBFP[46], as a reference for artifact correction. Future advances in expanding the spectra of 5-HT sensors (for example, far-red and near-infrared) will facilitate simultaneous monitoring of more neurochemicals and help disentangle their interactions with 5-HT.

When using sensors, optimizing the experimental system is crucial, which involves selecting the appropriate sensor with respect to various aspects, such as response, affinity and kinetics, as well as optimizing its expression level. It is also important to prevent disturbances of normal 5-HT levels. We intentionally used heterozygous SERT-cre mice[28] instead of homozygotes, because the homozygous SERT-KO mice showed markedly elevated basal levels of extracellular 5-HT, whereas heterozygotes exhibited similar levels[47].

In summary, our new 5-HT sensors can monitor 5-HT release both in vitro and in vivo, with high sensitivity and spatiotemporal resolution. When combined with advanced imaging techniques, they offer a powerful toolbox to study the serotonergic system in both health and disease.

Online content

Any methods, additional references, Nature Portfolio reporting summaries, source data, extended data, supplementary information, acknowledgements, peer review information; details of author contributions and competing interests; and statements of data and code availability are available at https://doi.org/10.1038/s41592-024-02188-8.

References

1. Berger, M., Gray, J. A. & Roth, B. L. The expanded biology of serotonin. *Annu. Rev. Med.* **60**, 355–366 (2009).
2. Li, Y. et al. Serotonin neurons in the dorsal raphe nucleus encode reward signals. *Nat. Commun.* **7**, 10503 (2016).
3. Portas, C. M. et al. On-line detection of extracellular levels of serotonin in dorsal raphe nucleus and frontal cortex over the sleep/wake cycle in the freely moving rat. *Neuroscience* **83**, 807–814 (1998).
4. Lesch, K. P. et al. Association of anxiety-related traits with a polymorphism in the serotonin transporter gene regulatory region. *Science* **274**, 1527–1531 (1996).
5. Theodore, W. H., Juhasz, C., Savic, V. & Drevets, W. Serotonin, depression, and epilepsy. *Epilepsia* **46**, 3 (2005).
6. Li, Y. et al. Synaptic mechanism underlying serotonin modulation of transition to cocaine addiction. *Science* **373**, 1252–1256 (2021).
7. Vaswani, M., Linda, F. K. & Ramesh, S. Role of selective serotonin reuptake inhibitors in psychiatric disorders: a comprehensive review. *Prog. Neuropsychopharmacol. Biol. Psychiatry* **27**, 85–102 (2003).
8. Fuller, R. W. Uptake inhibitors increase extracellular serotonin concentration measured by brain microdialysis. *Life Sci.* **55**, 163–167 (1994).
9. Lama, R. D., Charlson, K., Anantharam, A. & Hashemi, P. Ultrafast detection and quantification of brain signaling molecules with carbon fiber microelectrodes. *Anal. Chem.* **84**, 8096–8101 (2012).
10. Candelario, J. & Chachisvilis, M. Mechanical stress stimulates conformational changes in 5-hydroxytryptamine receptor 1B in bone cells. *Cell. Mol. Bioeng.* **5**, 277–286 (2012).
11. Wan, J. et al. A genetically encoded sensor for measuring serotonin dynamics. *Nat. Neurosci.* **24**, 746–752 (2021).
12. Dong, C. et al. Psychedelic-inspired drug discovery using an engineered biosensor. *Cell* **184**, 2779–2792 (2021).
13. Kubitschke, M. et al. Next generation genetically encoded fluorescent sensors for serotonin. *Nat. Commun.* **13**, 7525 (2022).
14. Unger, E. K. et al. Directed evolution of a selective and sensitive serotonin sensor via machine learning. *Cell* **183**, 1986–2002 (2020).
15. Guiard, B. P., El Mansari, M., Merali, Z. & Blier, P. Functional interactions between dopamine, serotonin and norepinephrine neurons: an in-vivo electrophysiological study in rats with monoaminergic lesions. *Int. J. Neuropsychopharmacol.* **11**, 625–639 (2008).
16. Jeong, S. et al. High-throughput evolution of near-infrared serotonin nanosensors. *Sci. Adv.* **5**, eaay3771 (2019).
17. Dana, H. et al. Sensitive red protein calcium indicators for imaging neural activity. *eLife* **5**, e12727 (2016).
18. Feng, J. et al. A genetically encoded fluorescent sensor for rapid and specific in vivo detection of norepinephrine. *Neuron* **102**, 745–761 (2019).
19. Sun, F. et al. Next-generation GRAB sensors for monitoring dopaminergic activity in vivo. *Nat. Methods* **17**, 1156–1166 (2020).
20. Bajar, B. T. et al. Improving brightness and photostability of green and red fluorescent proteins for live cell imaging and FRET reporting. *Sci. Rep.* **6**, 20889 (2016).
21. Pédelacq, J.-D., Cabantous, S., Tran, T., Terwilliger, T. C. & Waldo, G. S. Engineering and characterization of a superfolder green fluorescent protein. *Nat. Biotechnol.* **24**, 79–88 (2006).
22. Peng, Y. et al. 5-HT2C receptor structures reveal the structural basis of GPCR polypharmacology. *Cell* **172**, 719–730 (2018).
23. Ballesteros, J. A. & Weinstein, H. Integrated methods for the construction of three-dimensional models and computational probing of structure-function relations in G protein-coupled receptors. *Methods in Neurosciences* **25**, 366–428 (1995).
24. Wan, Q. et al. Mini G protein probes for active G protein-coupled receptors (GPCRs) in live cells. *J. Biol. Chem.* **293**, 7466–7473 (2018).
25. Kroeze, W. K. et al. PRESTO-Tango as an open-source resource for interrogation of the druggable human GPCRome. *Nat. Struct. Mol. Biol.* **22**, 362–369 (2015).
26. Zhuo, Y. et al. Improved green and red GRAB sensors for monitoring dopaminergic activity in vivo. *Nat. Methods* https://doi.org/10.1038/s41592-023-02100-w (2023).
27. Nagel, G. et al. Channelrhodopsin-2, a directly light-gated cation-selective membrane channel. *Proc. Natl Acad. Sci. USA* **100**, 13940–13945 (2003).
28. Zhuang, X., Masson, J., Gingrich, J. A., Rayport, S. & Hen, R. Targeted gene expression in dopamine and serotonin neurons of the mouse brain. *J. Neurosci. Methods* **143**, 27–32 (2005).

29. Broussard, G. J. et al. In vivo measurement of afferent activity with axon-specific calcium imaging. *Nat. Neurosci.* **21**, 1272–1280 (2018).

30. Xu, M. et al. Basal forebrain circuit for sleep–wake control. *Nat. Neurosci.* **18**, 1641–1647 (2015).

31. Oh, S. W. et al. A mesoscale connectome of the mouse brain. *Nature* **508**, 207–214 (2014).

32. Hamodi, A. S., Sabino, A. M., Fitzgerald, N. D., Moschou, D. & Crair, M. C. Transverse sinus injections drive robust whole-brain expression of transgenes. *eLife* **9**, e53639 (2020).

33. Ferezou, I. et al. Spatiotemporal dynamics of cortical sensorimotor integration in behaving mice. *Neuron* **56**, 907–923 (2007).

34. Klapoetke, N. C. et al. Independent optical excitation of distinct neural populations. *Nat. Methods* **11**, 338–346 (2014).

35. Wang, Q. X. et al. The allen mouse brain common coordinate framework: a 3D reference atlas. *Cell* **181**, 936–953 (2020).

36. Pasini, A., Tortorella, A. & Gale, K. The anticonvulsant action of fluoxetine in substantia nigra is dependent upon endogenous serotonin. *Brain Res.* **724**, 84–88 (1996).

37. Tecott, L. H. et al. Eating disorder and epilepsy in mice lacking 5-HT2C serotonin receptors. *Nature* **374**, 542–546 (1995).

38. Cheng, H.-M., Gao, C.-S., Lou, Q.-W., Chen, Z. & Wang, Y. The diverse role of the raphe 5-HTergic systems in epilepsy. *Acta Pharmacologica Sin.* **43**, 2777–2788 (2022).

39. Lin, W.-H. et al. Seizure-induced 5-HT release and chronic impairment of serotonergic function in rats. *Neurosci. Lett.* **534**, 1–6 (2013).

40. Dong, A. et al. A fluorescent sensor for spatiotemporally resolved imaging of endocannabinoid dynamics in vivo. *Nat. Biotechnol.* **40**, 787–798 (2021).

41. Ben-Ari, Y., Lagowska, J., Tremblay, E. & Le Gal La Salle, G. A new model of focal status epilepticus: intra-amygdaloid application of kainic acid elicits repetitive secondarily generalized convulsive seizures. *Brain Res.* **163**, 176–179 (1979).

42. Farrell, J. S. et al. In vivo assessment of mechanisms underlying the neurovascular basis of postictal amnesia. *Sci. Rep.* **10**, 14992 (2020).

43. Bunin, M. A. & Wightman, R. M. Quantitative evaluation of 5-hydroxytryptamine (serotonin) neuronal release and uptake: an investigation of extrasynaptic transmission. *J. Neurosci.* **18**, 4854–4860 (1998).

44. Thorré, K. et al. Differential effects of restraint stress on hippocampal 5-HT metabolism and extracellular levels of 5-HT in streptozotocin-diabetic rats. *Brain Res.* **772**, 209–216 (1997).

45. Hashemi, P., Dankoski, E. C., Petrovic, J., Keithley, R. B. & Wightman, R. M. Voltammetric detection of 5-hydroxytryptamine release in the rat brain. *Anal. Chem.* **81**, 9462–9471 (2009).

46. Subach, O. M. et al. Conversion of red fluorescent protein into a bright blue probe. *Chem. Biol.* **15**, 1116–1124 (2008).

47. Shen, H.-W. et al. Regional differences in extracellular dopamine and serotonin assessed by in vivo microdialysis in mice lacking dopamine and/or serotonin transporters. *Neuropsychopharmacology* **29**, 1790–1799 (2004).

Methods

Molecular biology

Plasmids were generated via Gibson assembly[48] and verified by Sanger sequencing (RuiBiotech). For the replacement-site screening, complementary DNAs encoding 12 5-HTR subtypes were cloned from the human GPCR cDNA library (hORFeome database 8.1) or the PRESTO-Tango GPCR Kit[25] (Addgene kit no. 1000000068). To optimize the 5-HT sensors, cDNAs encoding candidate sensors were cloned into the pDisplay vector (Invitrogen) with an IgK leader sequence in the sensor upstream, and either IRES-mCherry-CAAX (for green fluorescent 5-HT sensors) or IRES-EGFP-CAAX (for red fluorescent 5-HT sensors) was fused downstream of the sensor to calibrate the membrane signal. Site-directed mutagenesis was performed using primers containing randomized NNB codons (48 codons in total, encoding 20 possible amino acids). For expression in cultured neurons and mice in vivo, sequences of sensors were cloned into the pAAV vector (AAV information provided in Supplementary Table 1). To generate stable cell lines for measuring the excitation and emission spectra, sequences encoding sensors were cloned into a vector called pPacific, containing a 3′ terminal repeat, IRES, the puromycin gene and a 5′ terminal repeat. To measure downstream coupling using the Tango assay, DNA encoding various GRAB_{5-HT} sensors or wild-type 5-HTR4 was cloned into the pTango vector[25]. For the luciferase complementation assay, the β_2AR gene in the β2AR-Smbit construct[24] was replaced with the indicated GRAB_{5-HT} sensors or wild-type 5-HTR4; LgBit-mGs was a gift from N. A. Lambert (Augusta University).

Cell lines

HEK293T cells were purchased from ATCC (CRL-3216) and verified on the basis of their morphology and growth rate. Stable cell lines expressing different GRAB_{5-HT} sensors were generated by co-transfecting HEK293T cells with the pPacific plasmids encoding sensors and the pCS7-PiggyBAC plasmid encoding the transposase[49]. Cells expressing the desired genes were selected using 2 μg ml^{-1} puromycin (Sigma). An HTLA cell line stably expressing a tTA-dependent luciferase reporter and the β-arrestin2-TEV fusion gene used in the Tango assay[25] was a generous gift from B. L. Roth (University of North Carolina at Chapel Hill). All cell lines were cultured at 37 °C in 5% CO_2 in DMEM (Biological Industries) supplemented with 10% (vol/vol) fetal bovine serum (Gibco) and 1% penicillin–streptomycin (GIBCO).

Primary cultures

Rat cortical neurons were prepared using P0 Sprague–Dawley rat pups (both sexes) purchased from Beijing Vital River. The cerebral cortex was dissected, and neurons were dissociated using 0.25% trypsin-EDTA (Gibco), plated onto 12-mm glass coverslips coated with poly-D-lysine (Sigma-Aldrich) and cultured in neurobasal medium (Gibco) containing 2% B-27 supplement (Gibco), 1% GlutaMAX (Gibco) and 1% penicillin–streptomycin (Gibco) at 37 °C in humidified air containing 5% CO_2.

Animals

All procedures involving animals were performed using protocols approved by the Animal Care and Use Committee at Peking University. SERT-cre mice were generously provided by Y. Rao at Peking University. All mice were group- or pair-housed in a temperature-controlled (18–23 °C) and humidity-controlled (40–60%) room with a 12 h/12 h light/dark cycle, with food and water available ad libitum.

Cell transfection and imaging

HEK293T cells were plated either on 12-mm glass coverslips in 24-well plates or 96-well plates without coverslips and grown to ~70% confluence for transfection with PEI (1 μg plasmid and 3 μg PEI per well in 24-well plates, or 300 ng plasmids and 900 ng PEI per well in 96-well plates); the medium was replaced after 4–6 h, and the cells were used for imaging 24–48 h after transfection. After 5–9 d of in vitro culture, rat cortical neurons were infected with the indicated adeno-associated

viruses (AAVs). To compare the performance of various 5-HT sensors in Extended Data Fig. 3, each AAV was diluted to 2.53×10^{12} vg ml^{-1} and added at a volume of 1 μl well^{-1}.

Before imaging, the culture medium was replaced with Tyrode's solution consisting of (in mM): 150 NaCl, 4 KCl, 2 $MgCl_2$, 2 $CaCl_2$, 10 HEPES and 10 glucose (pH 7.4). Cells were imaged using an inverted Ti-E A1 confocal microscope (Nikon) or an Opera Phenix high-content screening system (PerkinElmer). The confocal microscope was equipped with a ×10/0.45 numerical aperture (NA) objective, a ×20/0.75 NA objective, a ×40/1.35 NA oil-immersion objective, a 488-nm laser, a 561-nm laser and the NIS-Element 4.51.00 software; the GFP signal was collected using a 525/50-nm emission filter combined with the 488-nm laser, and the RFP signal was collected using a 595/50-nm emission filter combined with the 561-nm laser. The Opera Phenix system was equipped with a ×20/0.4 NA objective, a ×40/1.1 NA water-immersion objective, a 488-nm laser, a 561-nm laser and the Harmony 4.9 software; the GFP and RFP signals were collected using a 525/50-nm and 600/30-nm emission filter, respectively. The fluorescence signals produced by the green and red fluorescent GRAB_{5-HT} sensors were calibrated using mCherry (the GFP/RFP ratio) or EGFP (the RFP/GFP ratio), respectively.

To measure the sensor responses induced by various chemicals, solutions containing the indicated chemicals were administered to the cells through a custom-made perfusion system or through bath application. To measure the sensors' kinetics, a glass pipette was positioned in close proximity to cells expressing the sensors, and the fluorescence signal was measured using the confocal high-speed line scanning mode, with a scanning speed of 1,024 Hz. To measure τ_{on}, 100 μM 5-HT was puffed from the pipette, and the increased trace in fluorescence was fitted with a single-exponential function; to measure τ_{off}, 100 μM RS 23597-190 was puffed on cells bathed in 10 μM 5-HT, and the decreased trace in fluorescence was fitted with a single-exponential function. To test for the potential blue-light-mediated photoactivation of the red fluorescent sensors, cells expressing r5-HT1.0 or jRGECO1a were imaged with the inverted Ti-E A1 confocal microscope; a 488-nm laser, with a duration of 1 s, was used as the stimulation light in imaging intervals. For the photoactivation shown in Fig. 1f, cells were illuminated by a 488-nm laser emitted from the objective (power, ~210 μW; intensity, ~0.4 W/cm^2). For results in Extended Data Fig. 1k,l, cells were illuminated by a 488-nm laser emitted from a fiber with a 200-μm diameter (maximal power, ~10 mW; intensity, ~32 W cm^{-2}).

Spectra measurements

For one-photon spectra, HEK293T cells stably expressing GRAB_{5-HT} sensors were collected and transferred to a 384-well plate in the absence or presence of 10 μM 5-HT. Excitation and emission spectra were measured at 5-nm increments with a 20-nm bandwidth using a Safire2 multi-mode plate reader (Tecan). Non-transfected cells were prepared to the same density as the cells that expressed sensors and were measured using the same protocol, for background subtraction.

For two-photon spectra, HEK293T cells expressing sensors were cultured on 12-mm coverslips and imaged using a two-photon microscope. The two-photon excitation laser was measured at 10-nm increments, and the laser power was calibrated for various wavelengths. For green sensors, excitation spectra were measured, ranging from 690 to 1,030 nm, using an Ultima Investigator two-photon microscope (Bruker) equipped with a ×20/1.0 NA water-immersion objective (Olympus), an InSight X3 tunable laser (Spectra-Physics) and the Prairie View 5.5 software (Bruker). For the red sensor, excitation spectra were measured, ranging from 820 to 1,300 nm, using an A1R MP+ multiphoton microscope (Nikon) equipped with a ×25/1.1 NA objective (Nikon) and a Chameleon Discovery tunable laser (Coherent).

Luciferase complementation assay

The luciferase complementation assay was performed as previously described[24]. In brief, 24–48 h after transfection, cells were washed with

PBS, dissociated using a cell scraper, resuspended in PBS, transferred to opaque 96-well plates containing 5 µM furimazine (NanoLuc Luciferase Assay, Promega) and bathed in 5-HT at various concentrations (ranging from 0.01 nM to 1 mM). After incubation for 10 min in the dark, luminescence was measured using a VICTOR X5 multilabel plate reader (PerkinElmer).

Tango assay

A reporter cell line called HTLA, stably expressing a tTA-dependent luciferase reporter and a β-arrestin2-TEV fusion gene, was transfected with pTango vectors to express GRAB$_{5-HT}$ sensors or wild-type 5-HTR4 or both GRAB$_{5-HT}$ sensors and 5-HTR4. After culturing for 24 h in 6-well plates, the cells were transferred to 96-well plates and bathed with 5-HT at varying concentrations (ranging from 0.01 nM to 100 µM). The cells were then cultured for 12 h to allow the expression of tTA-dependent luciferase. Bright-Glo reagent (Fluc Luciferase Assay System, Promega) was added to a final concentration of 5 µM, and luminescence was measured using a VICTOR X5 multilabel plate reader (PerkinElmer).

Behavior assays

Wild-type male C57BL/6J mice (6–8 weeks of age) were anesthetized with an i.p. injection of tribromoethanol (500 mg kg^{-1}) and placed on a stereotaxic frame (RWD Life Science). Then, 400 nl of the indicated AAVs (diluted to 1.86×10^{13} vg ml^{-1}) was unilaterally injected into the BA with the following coordinates: anterior–posterior (AP), −1.35 mm relative to bregma; medial–lateral (ML), ±3.0 mm; dorsal–ventral (DV), 4.5 mm below the dura, through a glass pipette using a micro-syringe pump (Nanoliter 2000 Injector, World Precision Instruments). Three weeks later, the same cohort of mice was subjected to various behavioral tests in the following order: elevated plus maze test, tail suspension test and forced swimming test. The behavior analysis was performed using the Smart 3.0 (Panlab) software.

Elevated plus maze test. The elevated plus maze comprises two opposite open arms (30 cm × 5 cm) without walls and two closed arms (30 cm × 5 cm × 15 cm) with opaque walls, and these four arms are connected by a central platform (5 × 5 cm). The maze is elevated 50 cm above the floor. At the beginning of each session, mice were placed in the center zone facing one of the open arms and were allowed to explore the maze for 5 min. Locomotion trajectories were recorded by a video camera. The arena was thoroughly cleaned with 75% ethanol between subjects. The time and entries in different zones were quantified and analyzed.

Tail suspension test. Each mouse was suspended by the tail ~40 cm above the floor, preventing any other contact or climbing during the assay. Then, a 6-min session was recorded, and the time spent immobile during a 2- to 6-min period was analyzed.

Forced swimming test. The mouse was placed in a transparent cylinder (12 cm in diameter and 30 cm in height), filled with water to a depth of 15 cm and maintained at 23–24 °C for a 6-min session recording. After each session, the mouse was dried with paper towels and returned to its home cage. The total immobility time during a 2- to 6-min period was analyzed. Mice were considered immobile when they did not make any active movements.

Fluorescence imaging of sensors in mouse acute brain slices

Wild-type male C57BL/6J mice (6–8 weeks of age) were anesthetized with an i.p. injection of tribromoethanol (500 mg kg^{-1}) and placed on a stereotaxic frame. Then the mixture of AAV9-hSyn-g5-HT3.0 (300 nl) and AAV9-hSyn-rDA3m (300 nl) was injected into the DRN (AP, −4.1 mm relative to bregma; ML, +1.1 mm; depth, 2.9 mm below the dura; at a 20° ML angle) at a rate of 50 nl min^{-1}. Three weeks after AAV injection, the mice were deeply anesthetized with tribromoethanol and perfused with 10 ml ice-cold oxygenated slicing buffer containing (in mM):

110 choline-Cl, 2.5 KCl, 0.5 CaCl$_2$, 7 MgCl$_2$, 1 NaH$_2$PO$_4$, 25 NaHCO$_3$, 25 glucose, 1.3 sodium ascorbate and 0.6 sodium pyruvate. Mice were then decapitated, and brains were rapidly removed and placed in cold (0–4 °C) oxygenated slicing buffer for 1 min. Next, brains were dissected for mounting to the cutting stage, and 300-µm-thick coronal slices were cut in ice-cold oxygenated slicing buffer using a VT1200 vibratome (Leica). The slices containing DRN were transferred and allowed to recover for at least 40 min at 34 °C in oxygenated artificial cerebrospinal fluid (ACSF) containing (in mM): 125 NaCl, 2.5 KCl, 2 CaCl$_2$, 1.3 MgCl$_2$, 1 NaH$_2$PO$_4$, 25 NaHCO$_3$, 25 glucose, 1.3 sodium ascorbate and 0.6 sodium pyruvate. For dual-color confocal imaging, the brain slices were then transferred to a custom-made perfusion chamber and imaged using an LSM710 confocal microscope (Zeiss), equipped with a ×20/0.5 NA water-immersion objective and the ZEN 2012 (Version 11.0.4.190) software. To minimize the spectral mixing, g5-HT3.0 and rDA3m were excited by a 488-nm laser and a 543-nm laser sequentially. The g5-HT3.0 and rDA3m signals were collected using detection wavelengths ranging from 509 nm to 558 nm and from 580 nm to 649 nm, respectively. For electrical stimulation, a homemade bipolar electrode (WE30031.0A3, MicroProbes) was placed onto the surface of the brain slice near the DRN expressing sensors. Electrical stimuli were applied using an S48 stimulator (Grass Instruments), with a stimulation voltage of 5–8 V and pulse duration of 1 ms. The frame scan was set to a size of 256 × 192 pixels with a speed of ~0.295 s per frame. For the spontaneous transients, the frame scan was set to a size of 512 × 512 pixels with a speed of ~1 s per frame, and the duration of each session was ~10 min.

Data for electrical stimuli were analyzed using custom programs written in ImageJ Macros and MATLAB. Data for spontaneous transients were preprocessed with Astrocyte Quantitative Analysis (AQuA)[50] and then analyzed using custom-written MATLAB programs and ImageJ macros.

Fiber-photometry recording of optogenetically evoked 5-HT release in vivo

To express the red fluorescent 5-HT sensors in the BF, adult SERT-cre mice were anesthetized with 1.5% isoflurane and placed on a stereotaxic frame. AAV9-hSyn-r5-HT1.0 or AAV9-hSyn-r5-HTmut was injected (400 nl) into the BF (AP, 0 mm relative to bregma; ML, +1.5 mm; DV, 4.6 mm below the dura). For optical activation of the DRN, 400 nl AAV9-EF1a-DIO-hChR2(H134R)-EYFP was injected into the DRN (AP, −4.1 mm relative to bregma; ML, +1.1 mm; depth, 2.9 mm below the dura; at a 20° ML angle). Two optical fiber cannulas (200 µm, 0.37 NA, Inper) were then implanted; one cannula was implanted 0.1 mm above the virus injection site in the BF to record the 5-HT sensor signals, and the other cannula was implanted 0.3 mm above the virus injection site in the DRN to optically activate ChR2. The optical fibers were affixed to the skull surface using dental cement. The fiber-photometry system (Inper) was used to record the fluorescence signals in freely moving mice. Yellow light-emitting diode (LED) light was bandpass filtered (561/10 nm), reflected by a dichroic mirror (495 nm) and then focused using a ×20 objective lens (Olympus). An optical fiber was used to guide the light between the commutator and the implanted optical fiber cannulas. The excitation light emitted by the LED was adjusted to 20–30 µW and delivered at 10 Hz with a 20-ms pulse duration. The optical signals were then collected through the optical fibers. Red fluorescence was bandpass filtered (520/20 nm and 595/30 nm) and collected using an sCMOS camera. To induce ChR2-mediated 5-HT release, pulse trains (10-ms pulses at 50 Hz for 1 s, 5 s or 10 s) were delivered to the DRN using a 488-nm laser at 10 mW with a 5-min inter-stimulus interval. To test the effects of fluoxetine on the ChR2-induced responses, three optical stimulation trains were applied at a 5-min interval. Then, 10 mg kg^{-1} fluoxetine was administered via i.p. injection; 30 min after injection, three optical stimulation trains were applied.

The current output from the photomultiplier tube was converted to a voltage signal using a model 1700 differential amplifier

(A-M Systems) and passed through a low-pass filter. The analog voltage signals were then digitized using an acquisition card (National Instruments). To minimize autofluorescence of the optical fibers, the recording fibers were photobleached using a high-power LED before recording. Background autofluorescence was recorded and subtracted from the recorded signals in the subsequent analysis.

The photometry data were analyzed using a custom program written in MATLAB. To calculate $\Delta F/F_0$ during the optogenetics experiments, a baseline was measured before optical stimulation.

Fiber-photometry recording of 5-HT dynamics during the sleep–wake cycle

Adult wild-type C57BL/6 mice or SERT-cre mice were anesthetized with isoflurane and placed on a stereotaxic frame for AAV injection (400 nl per site). In Fig. 3f–g, AAV9-hSyn-r5-HT1.0 or AAV9-hSyn-r5-HTmut was injected into the BF, and EF1α-DIO-axon-GCaMP6s was injected into the DRN of SERT-cre mice. In Extended Data Fig. 7a–c, AAV9-CAG-g5-HT1.0, diluted to 3.16×10^{12} vg ml^{-1}, was injected into the BF in one hemisphere, and AAV9-CAG-g5-HT3.0 was injected into the BF in another hemisphere, using the coordinates described above. In Extended Data Fig. 7d–f, AAV9-hSyn-PsychLight2 or AAV9-hSyn-g5-HT3.0 (diluted to 3.07×10^{12} vg ml^{-1}) was injected into the bilateral BF. In Extended Data Fig. 7g–i, AAV9-CAG-iSeroSnFR or AAV9-CAG-g5-HT3.0 (diluted to 2.15×10^{12} vg ml^{-1}) was injected into the bilateral BF. In Extended Data Fig. 7, wild-type C57BL/6 mice were used. An optical fiber cannula (200 μm, 0.37 NA, Inper) was implanted 0.1 mm above the virus injection site in BF to record sensor signals.

To assess the impact of viral titer on sensors' performance in vivo (Supplementary Fig. 2), according to the highest viral titers in our hands, AAVs with the indicated titers (including high, medium and low titers) were injected into the bilateral BF, as described above.

To record the animal's sleep–wake state, we attached and fixed custom-made EEG and EMG electrodes to the skull through a microconnector. EEG electrodes were implanted into craniotomy holes situated over the frontal cortex and visual cortex, and EMG wires were placed bilaterally in the neck musculature. The microconnector was attached to the skull using glue and a thick layer of dental cement. After surgery, the mice were allowed to recover for at least 2 weeks.

The same fiber-photometry system (Inper) was used to record the fluorescence signals in freely moving mice during sleep–wake cycles. In Fig. 3f,g, a 10-Hz 470/10-nm filtered light (20–30 μW) was used to excite the green fluorescent calcium sensor, and a 561/10-nm filtered light (20–30 μW) was used to excite the red fluorescent 5-HT sensors. Fluorescence signals were collected using a dual-band bandpass filter (520/20 nm and 595/30 nm), with excitation light delivered as 20-ms pulses at 10 Hz. In Extended Data Fig. 7, a 10-Hz 470/10-nm filtered light (20–30 μW) was used to excite the green fluorescent 5-HT sensors, and a 520/20-nm and 595/30 nm dual-band bandpass filter was used to collect the fluorescence signals.

Photometry data were analyzed using a custom MATLAB program. To calculate the $\Delta F/F_0$ during sleep–wake cycles, baseline values were measured during a period of REM sleep in which no apparent fluctuations were observed. To better quantify the fluorescence changes across multiple animals, the $\Delta F/F_0$ was further normalized using the s.d. of the baseline signals to get the z-score, with the formula: z-score = $\Delta F/F_0 / $ s.d.$_{baseline}$.

Fiber-photometry recording of 5-HT dynamics during reward, sensory stimuli and punishment conditions

Adult wild-type C57BL/6 mice were anesthetized with isoflurane and placed on a stereotaxic frame. In Extended Data Fig. 8a–d, 400 nl of AAV9-CAG-g5-HT1.0 (diluted to 3.16×10^{12} vg ml^{-1}) and CAG-g5-HT3.0 per site were injected bilaterally into the basal amygdala (BA) (AP, −1.35 mm relative to bregma; ML, ±3.0 mm; DV, 4.5 mm below the dura). In Extended Data Fig. 8e–g, AAV9-CAG-iSeroSnFR and CAG-g5-HT3.0

(diluted to 2.15×10^{12} vg ml^{-1}) were injected into the bilateral BA (400 nl per site). An optical fiber cannula (Inper) was implanted 0.1 mm above the virus injection sites in BA for recording the signals of 5-HT sensors.

Reward. An intraoral cheek fistula was implanted in each of the mice, which were given several days to recover. Mice were water-restricted for 36 h (until reaching 85% of initial body weight). Then water-restricted freely moving mice received 5% glucose water delivery (around 10 μl per trial, with 10 trials per session and a trial interval between 20 and 30 s).

Tone. The mouse was placed in a box with a loudspeaker, and a 2-s tone (5 kHz, 70 dB) was delivered for 10 trials, with a 30-s interval between trials.

The same fiber-photometry system (Inper) was used to record the fluorescence signals in freely moving mice during the sleep–wake cycle. In Extended Data Fig. 8, a 10-Hz 470/10-nm filtered light (20–30 μW) was used to excite green fluorescent 5-HT sensors. A 10-Hz 410/10-nm filtered light (20–30 μW) served as a control channel.

The fluorescence intensity of green 5-HT sensors excited by 410 nm and 470 nm was recorded as F_{410} and F_{470}, respectively. The $\Delta F/F_0$ was calculated under the above conditions using the formula: $\Delta F/F_0 = \Delta(F_{470}/F_{410}) / (F_{470}/F_{410})$. Baseline values were determined before the application of various stimuli. The z-score was computed as: z-score = $\Delta(F_{470}/F_{410}) / (F_{470}/F_{410}) / $ s.d.$_{baseline}$.

Polysomnographic recording and analysis

The sleep–wake state of each animal was determined using the EEG and EMG recordings. The EEG and EMG signals were amplified (NL104A, Digitimer), filtered (NL125/6, Digitimer) at 0.5–100 Hz (EEG) and 30–500 Hz (EMG), and then digitized using a Power1401 digitizer (Cambridge Electronic Design). The Spike2 software program (Cambridge Electronic Design) was used for recording, with a sampling rate of 1,000 Hz. The sleep–wake state was classified semi-automatically in 4-s epochs using AccuSleep[51] and then validated manually using a custom-made MATLAB GUI. The wake state was defined as desynchronized EEG activity combined with high EMG activity. NREM sleep was defined as synchronized EEG activity with high-amplitude delta activity (0.5–4 Hz) and low EMG activity. REM sleep was defined as high-power theta frequencies (6–9 Hz) combined with low EMG activity.

Mesoscopic in vivo imaging

To express the sensors throughout the cortex, we injected the indicated AAVs into the transverse sinus, as described previously[32]. In detail, P0–P1 C57BL/6 mouse pups were removed from their home cages, placed on a warm pad, anesthetized on ice for 2–3 min and fixed on an ice-cooled metal plate. Two small incisions were then made over the transverse sinuses for AAV injection using a glass pipette. For single-color imaging in the optogenetic experiments, AAV9-hSyn-g5-HT3.0 or AAV9-hSyn-EGFP-CAAX was injected bilaterally (4 μl total volume, 2 μl per hemisphere). For dual-color imaging, the pups were injected bilaterally with the following pairs of AAVs (6 μl total volume, 1:1): AAV9-hSyn-g5-HT3.0 and AAV9-hSyn-GAP43-jRGECO1a; AAV9-hSyn-r5-HT1.0 and AAV9-hSyn-eCB2.0; AAV9-hSyn-g5-HT3.0mut and AAV9-hSyn-GAP43-jRGECO1a; or AAV9-hSyn-r5-HTmut and AAV9-hSyn-eCB2.0. The AAVs were injected at a rate of 1.2 μl min^{-1}, and the pipette was left in the sinus for at least 30 s. After injection, the incisions were sealed with Vetbond glue (3 M Animal Care Products), and the pups were placed on a warm pad for recovery. After recovery, the pups were gently rubbed with bedding and returned to their home cage.

About 8 weeks after AAV injection, surgery was performed to implant the imaging window and the EEG and EMG electrodes. Anesthesia was induced with an i.p. injection of 2,2,2-tribromoethanol (500 mg kg^{-1}, Sigma-Aldrich) and maintained using inhalation with 1% isoflurane. The mouse was fixed in a stereotaxic frame, 2% lidocaine hydrochloride was injected under the scalp and the eyes were covered

with erythromycin ophthalmic ointment for protection. Part of the scalp above the skull and the underlying muscles were removed and cleaned to expose the skull. Most of the skull above the dorsal cortex was then removed and replaced with a flat custom-made coverslip (D-shape, ~8 mm × 8 mm) to create an optical window. EEG and EMG electrodes were implanted and fixed as described above. After surgery, the mice were returned to their home cage for at least 7 d to recover, and then were fixed to the base for more than 3 d to habituate before imaging; mice were habituated until they could fall asleep (and, in particular, could enter REM sleep) within the first 3 h. To optically activate the DRN, we used SERT-cre mice. As described above, except before the surgery, 300 nl AAV9-EF1a-DIO-ChrimsonR-iP2A-Halotag9-V5 was injected into the DRN (AP, −6.1 mm relative to bregma; ML, 0 mm relative to bregma; depth, 3 mm below the dura; at a 32° AP angle). To avoid the imaging window, the fiber was inserted forward and down from the back of the interparietal bone. An optical fiber cannula (Inper) was then implanted 0.2 mm above the virus injection site and affixed to the skull surface using dental cement.

Mesoscopic imaging was performed using a custom-made dual-color macroscope equipped with a ×2/0.5 NA objective lens (Olympus, MVPLAPO2XC), two ×1/0.25 NA tube lenses (Olympus, MVPLAPO1X) and two sCMOS cameras (Andor, Zyla 4.2 Plus, 2,048 × 2,048 pixels, 16-bit)[52,53]. Three excitation wavelengths (405 nm, 488 nm and 561 nm) were generated using a multi-line fiber coupled laser system (Changchun New Industries Optoelectronics, RGB-405/488/561/642nm-220mW-CC32594). The emission light was passed through a 567-nm cut-on longpass dichroic mirror (Thorlabs, DMLP567L), then through either a 525/36-nm or 609/34-nm emission filter (Chroma) into the sCMOS cameras. Both the excitation laser and the camera imaging were triggered by an Arduino board (Uno) with custom-written programs. Images were acquired using the Micro-Manager 2.0 software (NIH). For green sensor imaging, a 488-nm laser was used and interleaved with a 405-nm laser; for dual-color imaging, 488-nm and 561-nm lasers were simultaneously generated and interleaved with a 405-nm laser. Images were acquired using Micro-Manager 2.0 at a resolution of 512 × 512 pixels after 4× pixel binning, and each channel was acquired at either 1 Hz or 5 Hz with 40-ms exposure.

During imaging, the mice were head-fixed to the base and could freely run on a treadmill[54]. To induce ChrimsonR-mediated 5-HT release in the optogenetics experiment, pulse trains of light (10-ms pulses for 10 s at 5, 10, 20, 30, 40 or 50 Hz) were applied to the DRN using a 635-nm laser at 10 mW with a 3-min interval, and three trials were performed at each frequency. To test the effects of fluoxetine and GBR-12909 on ChrimsonR-evoked 5-HT release, three trains of optical stimulation (10-ms pulses for 1 s at 20 Hz, 10-ms pulses for 10 s at 20 Hz, or 10-ms pulses for 10 s at 50 Hz) were applied with a 5-min interval, and three trials were conducted for each parameter. Then, 10 mg kg^{-1} GBR-12909 was injected i.p., and the same optical stimulation procedure was performed 30 min later. Next, 20 mg kg^{-1} fluoxetine was injected i.p., followed by the same optical stimulation procedure 30 min later (Extended Data Fig. 9a). For the seizure experiments, an infrared camera was hung above the back of the mouse to record its behavioral data. After recording ~1 h of baseline data, 10 mg kg^{-1} KA was injected i.p. to induce seizures. All recordings, including mesoscopic imaging, EEG and EMG recording, optical stimulation trains and the infrared cameras, were synchronized using a Power1401 acquisition board (Cambridge Electronic Design).

Analysis of mesoscopic imaging data

Preprocessing. Raw images acquired by each camera were calibrated for the uniformity of the imaging system, and movement-related artifacts were corrected using the motion-correction algorithm NoRMCorre[55]. The corrected image stack, with a size of 512 × 512 pixels, was downsampled by a factor of 0.7, to 359 × 359 pixels, for subsequent analysis. For dual-color imaging, the averaged red-channel image was aligned with the averaged green-channel image through automatic transformation using the MATLAB function 'imregtform' with the 'similarity' mode. The same geometric transformation was applied to all red-channel images to align them to corresponding green-channel images. The image stack was saved as a binary file to accelerate the input and output of large files (typically >8 GB). To remove pixels belonging to the background and blood vessels (particularly large veins), we generated a mask for further analysis of the pixels. Specifically, the outline of the entire dorsal cortex in the field of view was generated manually, and pixels outside the outline were set as background and excluded from further analysis. The blood vessels were then removed from the image using the machine-learning-based ImageJ plugin Trainable Weka Segmentation[56] (v3.3.2) to minimize artifacts caused by the constriction and dilation of blood vessels. The final mask without the background and blood vessel pixels was applied to the image stack for further analysis.

Spectral unmixing. For simultaneous dual-color imaging, the bleed-through of fluorescence intensity for each pixel between the green and red channels was removed using linear unmixing[57] on the basis of the spectra of the various sensors and the setup of the microscope system. Specifically, the proportion of fluorescence intensities detected by two cameras for various sensors was calculated on the basis of sensors' emission spectra and the bandpass of filters. The value of each pixel in preprocessed images was recalculated on the basis of these ratios for linear unmixing with following equations:

$$F'_G = F_G + F_R \times C_G \tag{1}$$

$$F'_R = F_R + F_G \times C_R \tag{2}$$

F_G and F_R indicate the real fluorescence intensity of the pixel in green and red channels, respectively; F_G' and F_R' indicate the measured fluorescence intensity of the pixel in green and red channels, respectively; and C_G and C_R indicate the bleed-through ratio in the green channel (from red sensors) and the red channel (from green sensors), respectively. And we can get the exact value of F_G and F_R based on other values, including F_G', F_R', C_G and C_R, with following formulas:

$$F_G = (F'_G - F'_R \times C_G)/(1 - C_G \times C_R) \tag{3}$$

$$F_R = (F'_R - F'_G \times C_R)/(1 - C_G \times C_R) \tag{4}$$

The images after spectral unmixing were used for further analysis.

Hemodynamic correction and response calculation. Hemodynamic changes can affect the absorption of light, resulting in changes in fluorescence[58,59]. According to the spectra of the sensors, when excited with 405-nm light, the g5-HT3.0, eCB2.0, r5-HT1.0 and jRGECO1a sensors are ligand-insensitive, which can reflect hemodynamic absorption. To correct for hemodynamic artifacts, we performed a pixel-by-pixel correction on the basis of linear regression[60] of the ligand-dependent signals (excited by 488 nm or 561 nm) against the ligand-independent signals (excited by 405 nm). The baseline images were spatially smoothed using a Gaussian filter ($\sigma = 2$) and used for the linear regression. Then, for each pixel, the baseline fluorescence intensity of the 405-nm excited channel was regressed onto the 488-nm or 561-nm signal, obtaining regression coefficients for rescaling the 405-nm channel. The rescaled 405-nm signal was subtracted from the 488-nm or 561-nm signal to generate a corrected signal for each pixel. To avoid the corrected signal becoming close to zero, or even less than zero, the corrected signal was added to the average rescaled 405-nm channel signal as the final corrected signal of fluorescence intensity for the response calculation. The response of each pixel was calculated using the equation $\Delta F/F_0 = (F - F_0)/F_0$, where F_0 is defined as the average

baseline fluorescence intensity. When analyzing the data obtained during sleep–wake cycles, the baseline was defined as the REM sleep state, in which the signal had no apparent fluctuation.

Parcellation of cortical areas. On the basis of previous studies[61,62], we rigidly registered the average fluorescence image to a two-dimensional projection of the Allen Common Coordinate Framework v3 (CCFv3) using four manually labeled anatomical landmarks, namely the left, center and right points in the boundary between the anterior cortex and the olfactory bulbs, and the medial point at the base of the retrosplenial cortex. To analyze the time series response in an individual brain region, we averaged the $\Delta F/F_0$ value for all available pixels within that brain region. To obtain the average response map from multiple mice (Fig. 4g), we developed a custom code to first register the response image for each individual mouse to the Allen CCFv3, and then averaged the images, keeping only the intersection among all mice. For the analysis of serotonergic projection in the mouse dorsal cortex, the serotonergic projection map was modified from Allen Mouse Brain Connectivity Atlas (connectivity.brain-map.org/projection/experiment/cortical_map/480074702).

Analysis of propagating waves

Peak response calculation. The time series of the images obtained before (~30 s before the wave originated), during and after (~30 s after the wave disappeared) wave propagation was extracted as an event for further analysis. Images taken during the first 20 s (20 frames) were set as the event baseline. The event response image was spatially filtered, and each pixel during the event was then corrected to set the average response of the event baseline to zero. The peak response site was automatically found by a circle with a 500-μm diameter across the event, and its average value was defined as the peak response of the event.

Identification of wave directions using optical flow analysis. To determine the direction of the waves, we adopted an optical flow method to automatically detect the wave directions on the basis of the NeuroPatt toolbox[63]. In detail, the corrected response image stack was smoothed over time, downsampled in size by a factor of 0.2, and normalized to the maximum response for each pixel. The phase velocity fields were then calculated using the 'opticalFlowHS' MATLAB function (smoothness parameter $\alpha = 0.05$). For each frame, velocity fields were ignored in pixels with a low response, defined as smaller than threefold s.d. of the baseline. Finally, we obtained the frequency distribution of these wave directions in each event and the average distribution of all events (see Fig. 5h).

Calculation of wave speed. The velocity fields calculated using the optical flow method depend on two parameters[63] and tend to be underestimated; therefore, we used a different method to calculate the speed of waves (see Extended Data Fig. 10e). In detail, the time (T) to peak response for each pixel was determined, and the pixel with the shortest time (T_0) to reach the peak response was defined as the origin. The wave-propagating region was then divided by fans centered at the origin with 0.5° intervals, and the relative distance (ΔS) between the distal pixel and the origin was calculated. The speed (v) in each direction was then calculated using the equation $v = \Delta S / (T - T_0)$. Finally, we obtained the frequency distribution for speed in each event and the average distribution of all events (see Fig. 5h).

Quantification and statistical analysis

Where appropriate, cells or animals were randomly assigned to either the control or experimental group. Imaging data were processed using ImageJ (1.53q) software (NIH) and custom-written MATLAB (R2020b) programs. Data were plotted using OriginPro 2020b (Originlab) or Adobe Illustrator CC. Except where indicated, all summary data are reported as the mean ± s.e.m. The SNR was calculated as the peak response divided by the s.d. of the baseline fluorescence fluctuation.

All data were assumed to be distributed normally, and equal variances were formally tested. Differences were analyzed using the two-tailed Student's t-test or one-way ANOVA; $^*P < 0.05$, $^{**}P < 0.01$, $^{***}P < 0.001$, and n.s., not significant ($P \geq 0.05$).

Reporting summary

Further information on research design is available in the Nature Portfolio Reporting Summary linked to this article.

Data availability

The plasmids used to express the sensors in this study and the related sequences are available from Addgene (catalog nos. 208709–208727; https://www.addgene.org/Yulong_Li/). The human GPCR cDNA library was obtained from the hORFeome database 8.1 (http://horfdb.dfci.harvard.edu/index.php?page=home). Source data are provided with this paper.

Code availability

The custom-written MATLAB, Arduino and ImageJ programs are available under an MIT license from https://github.com/yulonglilab.

References

48. Gibson, D. G. et al. Enzymatic assembly of DNA molecules up to several hundred kilobases. *Nat. Methods* **6**, 343–345 (2009).
49. Yusa, K., Zhou, L., Li, M. A., Bradley, A. & Craig, N. L. A hyperactive piggyBac transposase for mammalian applications. *Proc. Natl Acad. Sci. USA* **108**, 1531–1536 (2011).
50. Wang, Y. et al. Accurate quantification of astrocyte and neurotransmitter fluorescence dynamics for single-cell and population-level physiology. *Nat. Neurosci.* **22**, 1936–1944 (2019).
51. Barger, Z., Frye, C. G., Liu, D. Q., Dan, Y. & Bouchard, K. E. Robust, automated sleep scoring by a compact neural network with distributional shift correction. *PLoS ONE* **14**, e0224642 (2019).
52. Werley, C. A., Chien, M. P. & Cohen, A. E. Ultrawidefield microscope for high-speed fluorescence imaging and targeted optogenetic stimulation. *Biomed. Opt. Express* **8**, 5794–5813 (2017).
53. Zhuang, C. et al. Real-time brain-wide multi-planar microscopy for simultaneous cortex and hippocampus imaging at the cellular resolution in mice. *Biomed. Opt. Express* **12**, 1858–1868 (2021).
54. Jackson, J., Karnani, M. M., Zemelman, B. V., Burdakov, D. & Lee, A. K. Inhibitory control of prefrontal cortex by the claustrum. *Neuron* **99**, 1029–1039 (2018).
55. Pnevmatikakis, E. A. & Giovannucci, A. NoRMCorre: an online algorithm for piecewise rigid motion correction of calcium imaging data. *J. Neurosci. Methods* **291**, 83–94 (2017).
56. Arganda-Carreras, I. et al. Trainable Weka Segmentation: a machine learning tool for microscopy pixel classification. *Bioinformatics* **33**, 2424–2426 (2017).
57. Zimmermann, T. Spectral imaging and linear unmixing in light microscopy. *Adv. Biochem Eng. Biotechnol.* **95**, 245–265 (2005).
58. Ma, Y. et al. Wide-field optical mapping of neural activity and brain haemodynamics: considerations and novel approaches. *Philos. Trans. R. Soc. B Biol. Sci.* **371**, 20150360 (2016).
59. Valley, M. T. et al. Separation of hemodynamic signals from GCaMP fluorescence measured with wide-field imaging. *J. Neurophysiol.* **123**, 356–366 (2020).
60. Vesuna, S. et al. Deep posteromedial cortical rhythm in dissociation. *Nature* **586**, 87–94 (2020).
61. Musall, S., Kaufman, M. T., Juavinett, A. L., Gluf, S. & Churchland, A. K. Single-trial neural dynamics are dominated by richly varied movements. *Nat. Neurosci.* **22**, 1677–1686 (2019).
62. Saxena, S. et al. Localized semi-nonnegative matrix factorization (LocaNMF) of widefield calcium imaging data. *PLoS Comput. Biol.* **16**, e1007791 (2020).

63. Townsend, R. G. & Gong, P. Detection and analysis of spatiotemporal patterns in brain activity. *PLoS Comput. Biol.* **14**, e1006643 (2018).

Author contributions

Competing interests

The authors declare no competing interests.

Additional information

Extended data is available for this paper at https://doi.org/10.1038/s41592-024-02188-8.

Supplementary information The online version contains supplementary material available at https://doi.org/10.1038/s41592-024-02188-8.

Correspondence and requests for materials should be addressed to Yulong Li.

Peer review information *Nature Methods* thanks Sanghwa Jeong and the other, anonymous, reviewer(s) for their contribution to the peer review of this work. Peer reviewer reports are available. Primary Handling Editor: Nina Vogt, in collaboration with the *Nature Methods* team.

Reprints and permissions information is available at www.nature.com/reprints.
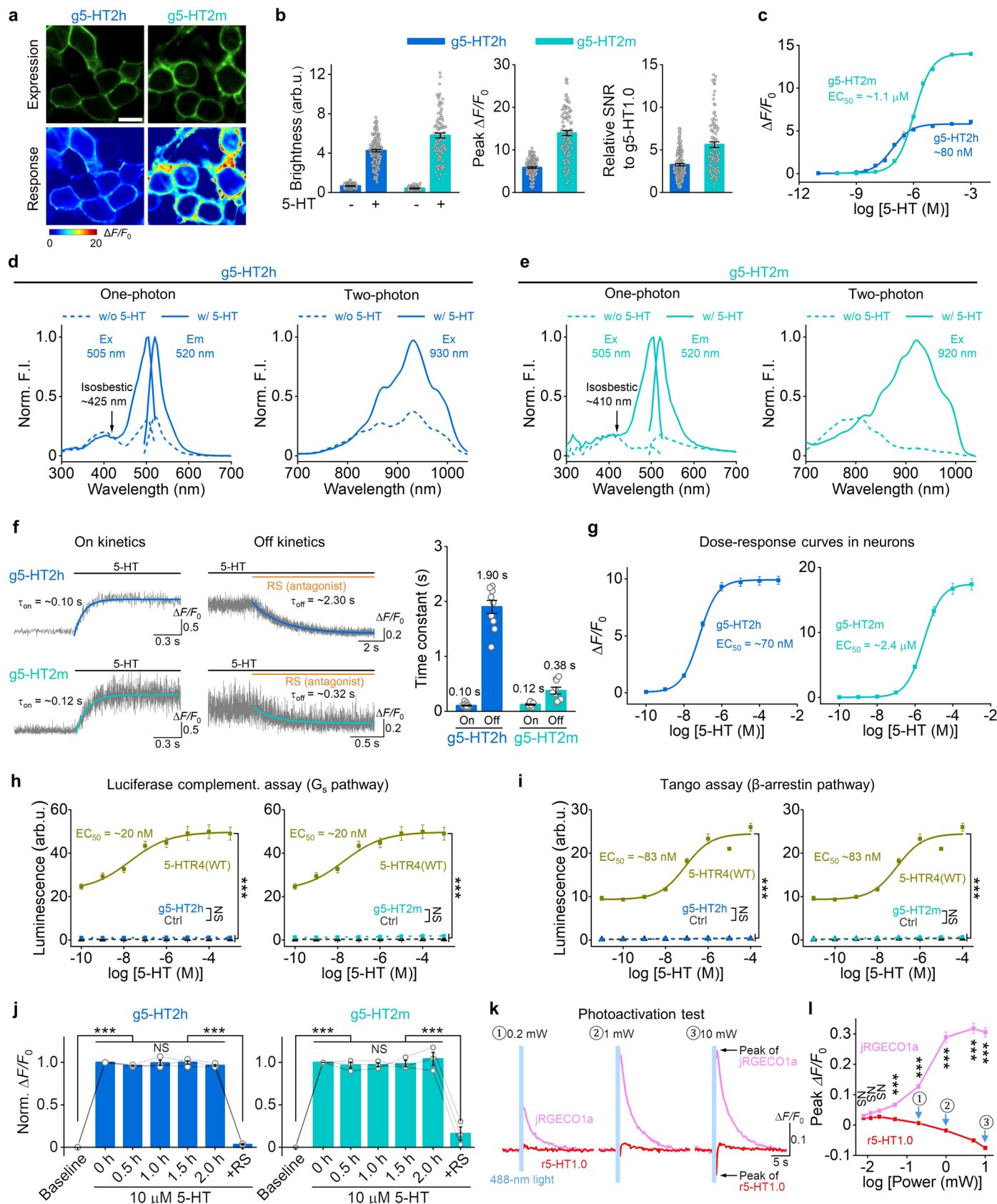
**Extended Data Fig. 1 | See next page for caption.**

Extended Data Fig. 1 | Characterization of GRAB$_{5-HT}$ sensors in HEK293T cells and cultured rat cortical neurons. a, Representative images showing the expression (top, with 5-HT) and responses (bottom) to 100 μM 5-HT for g5-HT2h (left) and g5-HT2m (right). Scale bar, 20 μm. **b**, The group summary of the brightness (left), peak $\Delta F/F_0$ (middle) and SNR (right) of g5-HT2h and g5-HT2m. The SNR is relative to g5-HT1.0; arb.u., arbitrary units. n = 154 cells from 3 coverslips (short for 154/3) for g5-HT2h, 98/3 for g5-HT2m. **c**, Dose-dependent curves of g5-HT2h and g5-HT2m. n = 3 wells for each sensor with 300–500 cells per well. **d**–**e**, Excitation (Ex) and emission (Em) spectra of g5-HT2h (**d**) and g5-HT2m (**e**) in the absence (dash line) and presence of 10 μM 5-HT (solid line) under one-photon (left), and two-photon excitation (right). w/o, without; w/, with. **f**, Representative traces of sensor fluorescence increase to 5-HT puffing and decrease to RS puffing (left). Group summary of on and off kinetics (right). n = 16 cells from 4 coverslips (16/4) for g5-HT2h on kinetics, 10/3 for g5-HT2h off kinetics, 11/3 for g5-HT2m on kinetics, 9/3 for g5-HT2m off kinetics. **g**, Dose-response curves of g5-HT2h (left) and g5-HT2m (right) in cultured rat cortical neurons. n = 60 ROIs from 3 coverslips for g5-HT2h and g5-HT2m. **h**–**i**, Downstream coupling tests of g5-HT2h and g5-HT2m for G$_s$ coupling (**h**) and β-arrestin coupling (**i**). Data of WT and Ctrl groups were replotted from Fig. 2l. n = 3 wells per group with 200–500 cells per well. One-way ANOVA followed by

Tukey's multiple-comparison tests, in panel **h**, post hoc test in 1 mM 5-HT: P = 2.65 × 10^{-6} and 0.96 for g5-HT2h versus WT and Ctrl, respectively, P = 2.93 × 10^{-6} and 0.82 for g5-HT2m versus WT and Ctrl, respectively; in panel **i**, post hoc test: P = 4.94 × 10^{-8} and 1 for g5-HT2h versus WT and Ctrl, respectively, P = 5.96 × 10^{-8} and 0.88 for g5-HT2m versus WT and Ctrl, respectively. **j**, The fluorescence of g5-HT2h (left) and g5-HT2m (right) expressed in cultured rat cortical neurons in response to a 2-h application of 5-HT, followed by RS. n = 3 wells for each sensor. One-way repeated measures ANOVA followed by Tukey's multiple-comparison tests, for g5-HT2h, F = 670, P = 2.83 × 10^{-5}, post hoc test: P = 0 for baseline versus 0 h, P = 0 for 2.0 h versus RS, P = 0.76, 1, 1, 0.80 for 0 h versus 0.5 h, 1 h, 1.5 h or 2.0 h, respectively; for 5-HT2m, F = 100.3, P = 0.006, post hoc test: P = 1.13 × 10^{-6} for baseline versus 0 h, P = 1.77 × 10^{-7} for 2.0 h versus RS, P = 1, 1, 1, 0.99 for 0 h versus 0.5 h, 1 h, 1.5 h or 2.0 h, respectively. **k**, Averaged traces of jRGECO1a and r5-HT1.0 in response to 0.2, 1 and 10-mW blue light, respectively. **l**, Blue light intensity-dependent peak $\Delta F/F_0$ curves of jRGECO1a or r5-HT1.0. n = 37/2 for jRGECO1a and 49/2 for r5-HT1.0 in **k**, **l**. Two-way ANOVA followed by Tukey's multiple-comparison tests, for jRGECO1a versus r5-HT1.0 under indicated blue light power, P = 1, 0.9761, 0.8783, 5.22 × 10^{-4}, 0, 0, 0 and 0, respectively. Data are shown as mean ± s.e.m. in **b**,**c**,**f**–**l**, with the error bars indicating the s.e.m. ***P < 0.001, n.s., not significant.
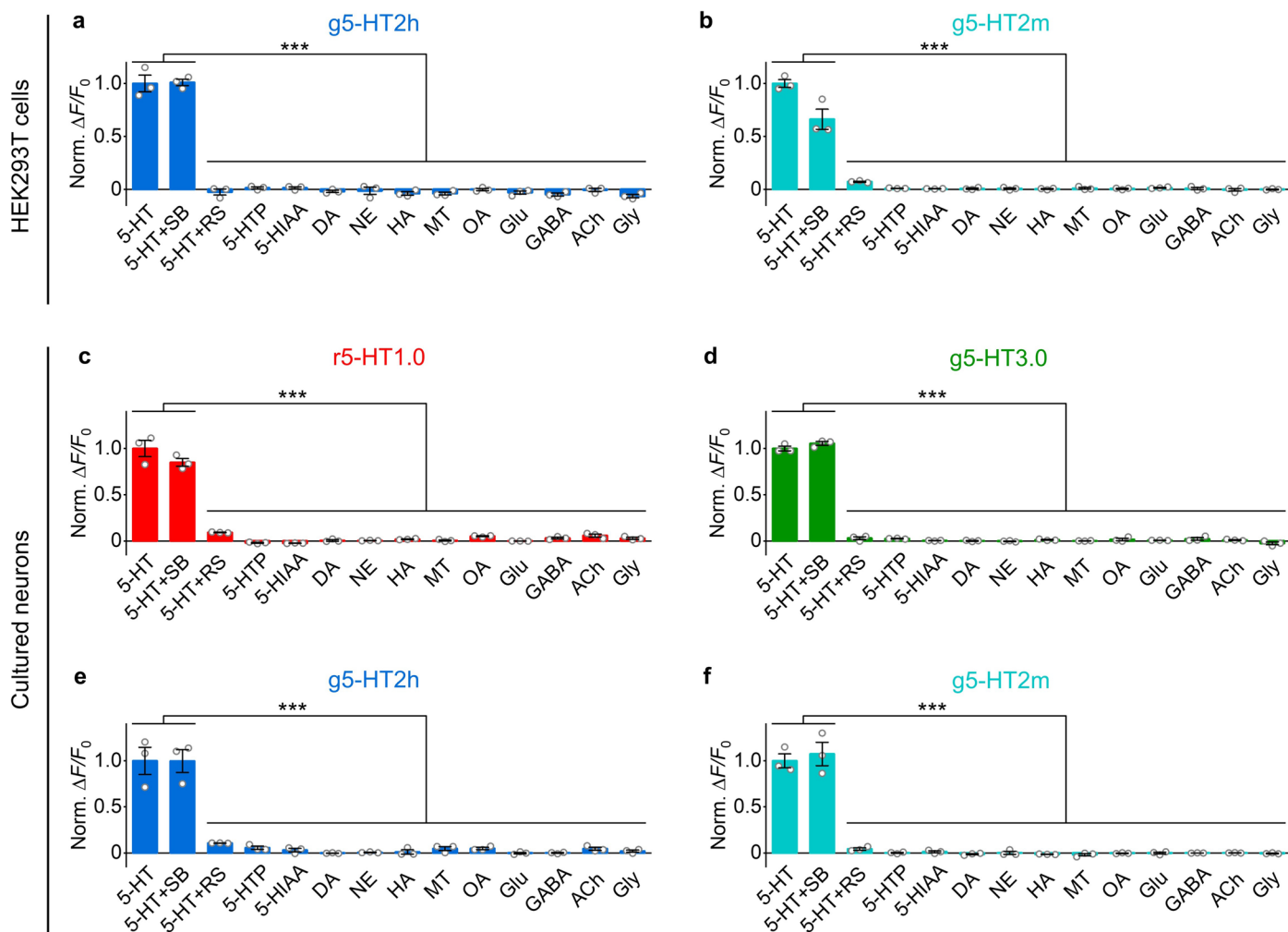
Extended Data Fig. 2 | Specificity of 5-HT sensors. Specificity test of indicated sensors in HEK293T cells (**a**, **b**) or cultured rat cortical neurons (**c–f**) to 5-HT alone, 5-HT together with SB, 5-HT together with RS, and 5-HT precursor, 5-HT metabolites, as well as other neurotransmitters and neuromodulators (all compounds at 10 μM except RS at 100 μM). 5-HTP, 5-hydroxytryptophan; 5-HIAA, 5-hydroxyindole acetic acid; DA, dopamine; NE, norepinephrine; HA, histamine; MT, melatonin; OA, octopamine; Glu, glutamate; GABA, gamma-aminobutyric acid; ACh, acetylcholine; Gly, glycine. Norm., normalized. $n = 3$ wells for each group with 200–500 cells per well. One-way ANOVA followed by Tukey's multiple-comparison tests, in panel **a**, $F_{13,28} = 180.2$, $P = 2.08 \times 10^{-23}$, post hoc test: $P = 0$ for 5-HT versus 5-HT and RS, and other compounds; in panel **b**, $F_{13,28} = 120$,

$P = 5.52 \times 10^{-21}$, post hoc test: $P = 0$ for 5-HT versus 5-HT and RS, and other compounds; in panel **c**, $F_{13,28} = 148.9$, $P = 2.86 \times 10^{-22}$, post hoc test: $P = 0$ for 5-HT versus 5-HT and RS, and other compounds; in panel **d**, $F_{13,28} = 918$, $P = 3.16 \times 10^{-33}$, post hoc test: $P = 0$ for 5-HT versus 5-HT and RS, and other compounds; in panel **e**, $F_{13,28} = 44.2$, $P = 3.65 \times 10^{-15}$, post hoc test: $P = 4.39 \times 10^{-7}$, 2.06×10^{-7}, 9.18×10^{-8}, 1.26×10^{-7}, 1.26×10^{-7}, 1.26×10^{-7}, 2.08×10^{-7}, 2.08×10^{-7}, 1.26×10^{-7}, 1.26×10^{-7}, 2.09×10^{-7} and 9.18×10^{-8} for 5-HT versus 5-HT and RS, and 5-HTP, 5-HIAA, DA, NE, HA, MT, OA, Glu, GABA, ACh and Gly; in panel **f**, $F_{13,28} = 87.9$, $P = 3.83 \times 10^{-19}$, post hoc test: $P = 1.75 \times 10^{-9}$, 0, 2.33×10^{-11}, 0, 0, 0, 0, 0, 0, 0 and 0 for 5-HT versus 5-HT and RS, and 5-HTP, 5-HIAA, DA, NE, HA, MT, OA, Glu, GABA, ACh and Gly. Data are shown as mean ± s.e.m., with the error bars indicating the s.e.m. ***$P < 0.001$.
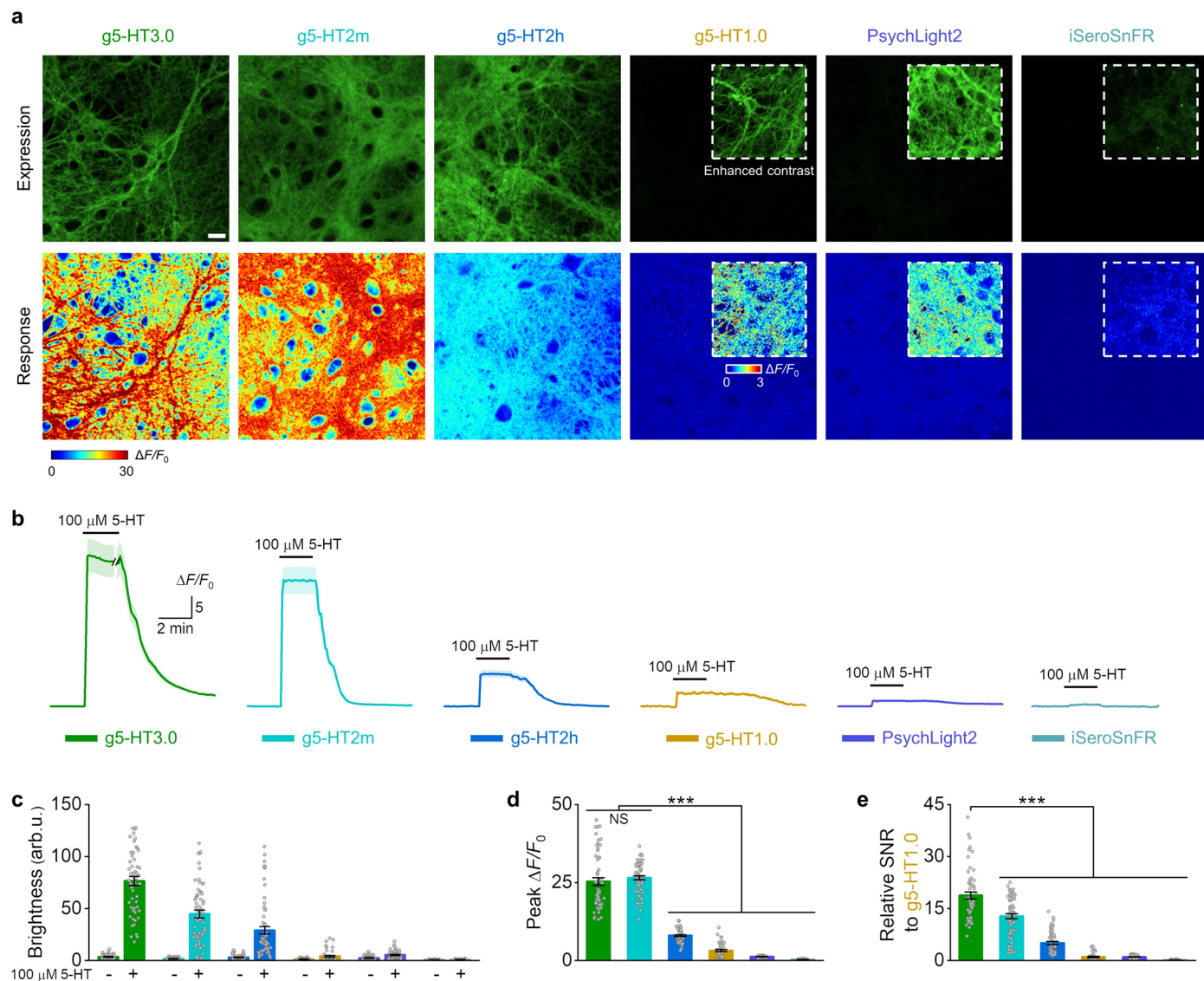
Extended Data Fig. 3 | Comparison of single GFP-based 5-HT sensors in cultured rat cortical neurons. a, Representative images showing the fluorescence expression (top) and responses (bottom) to 100 μM 5-HT for different sensors as indicated. Insets with white dashed outlines in images have either enhanced contrast (top) or different pseudocolor scales (bottom). Similar results were observed for more than 30 neurons. Scale bar, 20 μm. **b**, Representative traces in response to 100 μM 5-HT for different sensors as indicated. **c–e**, Group summary of the brightness (**c**), peak $\Delta F/F_0$ (**d**) and SNR (**e**). The SNR of all sensors is relative to the SNR of g5-HT1.0; arb.u., arbitrary units, the basal brightness of g5-HT1.0 was set to 1. $n = 56$ ROIs from 3 coverslip (short for 56/3) for g5-HT3.0, 60/3 for g5-HT2m, 60/3 for g5-HT2h, 48/3 for g5-HT1.0, 60/3

for PsychLight2 and 60/3 for iSeroSnFR. One-way ANOVA followed by Tukey's multiple-comparison tests for **d,e**. For peak $\Delta F/F_0$ in **d**, $F_{5,338} = 446.9$, $P = 1.46 \times 10^{-146}$, post hoc test: $P = 0.696$, 7.75×10^{-9}, 1.01×10^{-8}, 0 and 0 for g5-HT3.0 versus g5-HT2m, g5-HT2h, g5-HT1.0, PsychLight2 and iSeroSnFR; $P = 8.8 \times 10^{-9}$, 1.6×10^{-8}, 0 and 2.49×10^{-8} for g5-HT2m versus g5-HT2h, g5-HT1.0, PsychLight2 and iSeroSnFR. For relative SNR in **e**, $F_{5,338} = 195.1$, $P = 2.46 \times 10^{-97}$, post hoc test: $P = 7.55 \times 10^{-9}$, 0, 7.92×10^{-9}, 8.66×10^{-9} and 6.64×10^{-8} for g5-HT3.0 versus g5-HT2m, g5-HT2h, g5-HT1.0, PsychLight2 and iSeroSnFR. Data are shown as mean ± s.e.m. in **b–e**, with the error bars or shaded regions indicating the s.e.m. ***$P < 0.001$, n.s., not significant.
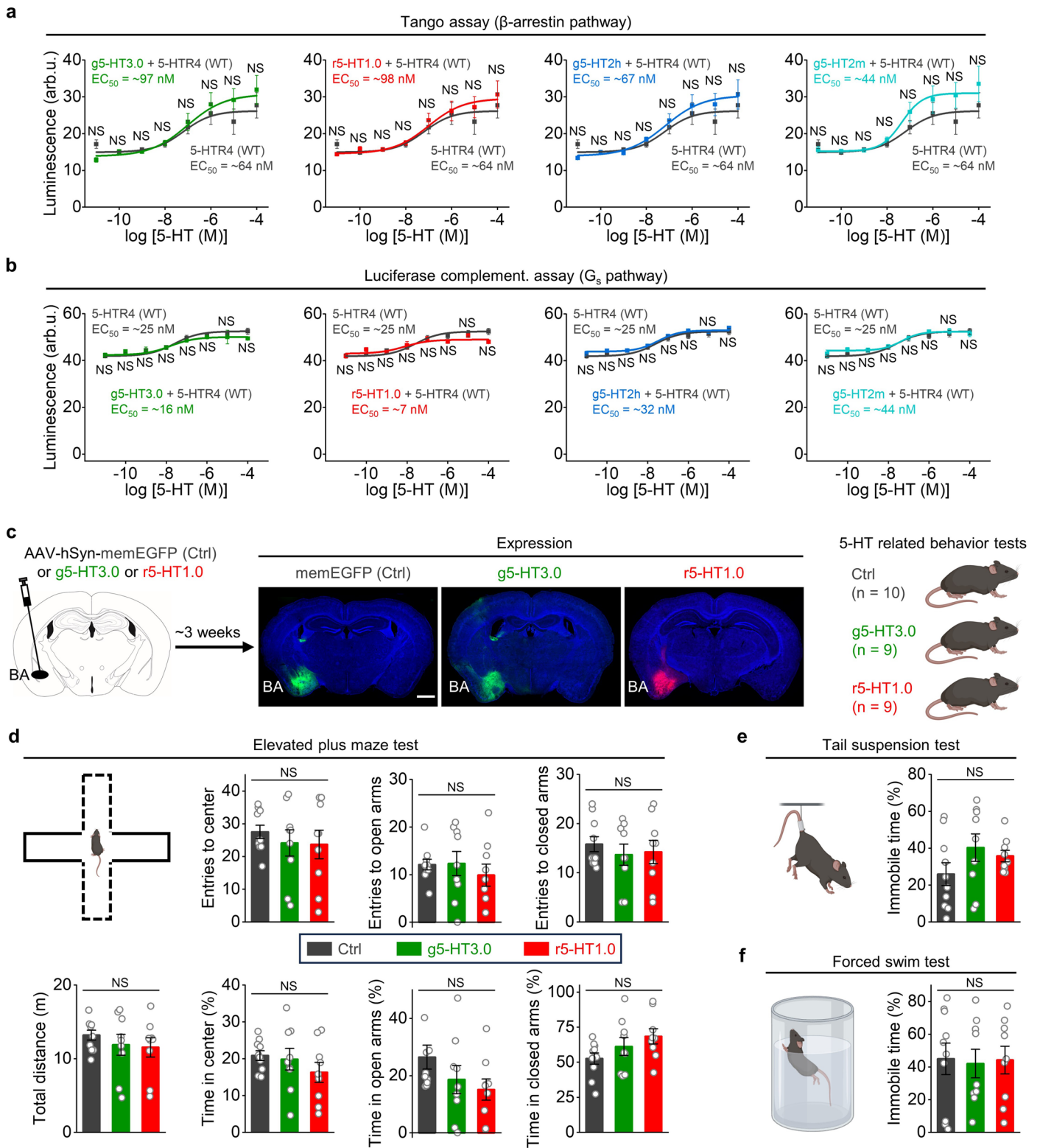
Extended Data Fig. 4 | See next page for caption.

Extended Data Fig. 4 | Expression of GRAB$_{5\text{-}HT}$ sensors shows minimal buffering effects. a–b, *In vitro* test of buffering effects according to downstream coupling tests for β-arrestin coupling (**a**) and G$_s$ coupling (**b**). n = 9 wells from three independent cultures per group with 200–500 cells per well. WT, wild type (the same WT results were used for different sensors in each assay); arb.u., arbitrary units. Two-way ANOVA tests were performed followed by Tukey's multiple-comparison tests. In panel **a**, for g5-HT3.0 + 5-HTR4 versus 5-HTR4 only, P = 0.9877, 1, 1, 1, 1, 1, 0.8698 and 0.9888 in the application of 5-HT concentration from 10^{-11} to 10^{-4} M, respectively; for r5-HT1.0 + 5-HTR4 versus 5-HTR4 only, P = 0.9999, 1, 1, 1, 1, 1, 0.9929 and 0.9996; for g5-HT2h + 5-HTR4 versus 5-HTR4 only, P = 0.9956, 1, 1, 1, 1, 1, 0.9722 and 0.9997; for g5-HT2m + 5-HTR4 versus 5-HTR4 only, P = 1, 1, 1, 1, 0.9968, 0.9987, 0.7619 and 0.9252. In panel **b**, for g5-HT3.0 + 5-HTR4 versus 5-HTR4 only, P = 1, 1, 1, 1, 1, 1, 1 and 0.8968; for r5-HT1.0 + 5-HTR4 versus 5-HTR4 only, P = 1, 0.9755, 1, 1, 1, 0.9177, 1 and 0.104; for g5-HT2h + 5-HTR4 versus 5-HTR4 only, P = 1, 0.9972, 1, 1, 1, 0.9349, 1 and 0.9984; for g5-HT2m + 5-HTR4 versus 5-HTR4 only, P = 1, 0.9906, 1, 1, 1, 0.9981, 1 and 1.

c–f, *In vivo* test of buffering effects using multiple 5-HT related behavior tests. n = 10, 9 and 9 mice for the Ctrl, g5-HT3.0 and r5-HT1.0 group, respectively. **c**, Schematic illustrates the AAV injections of memEGFP (control) or g5-HT3.0 or r5-HT1.0 in mice basal amygdala (BA) (left); representative images exhibit the corresponding expression, scale bar, 1 mm (middle); cartoon shows mice for 5-HT related behavior tests (right). **d–f**, Schematic illustration (left) and quantification of behavioral parameters (right) in the elevated plus maze test (**d**), the tail suspension test (**e**) and the forced swim test (**f**). One-way ANOVA tests were performed. In panel **d**, $F_{2,25}$ = 0.366, P = 0.6975 for entries to center; $F_{2,25}$ = 0.433, P = 0.6534 for entries to open arms; $F_{2,25}$ = 0.3078, P = 0.7378 for entries to closed arms; $F_{2,25}$ = 0.5944, P = 0.5595 for total distance; $F_{2,25}$ = 1.0191, P = 0.3754 for time in center; $F_{2,25}$ = 1.8749, P = 0.1743 for time in open arms; $F_{2,25}$ = 2.3079, P = 0.1203 for time in closed arms. In panel **e**, $F_{2,25}$ = 1.5753, P = 0.2268. In panel **f**, $F_{2,25}$ = 0.0281, P = 0.9723. Data are shown as mean ± s.e.m. in **a–b**, **d–f**, with the error bars indicating the s.e.m. n.s., not significant.
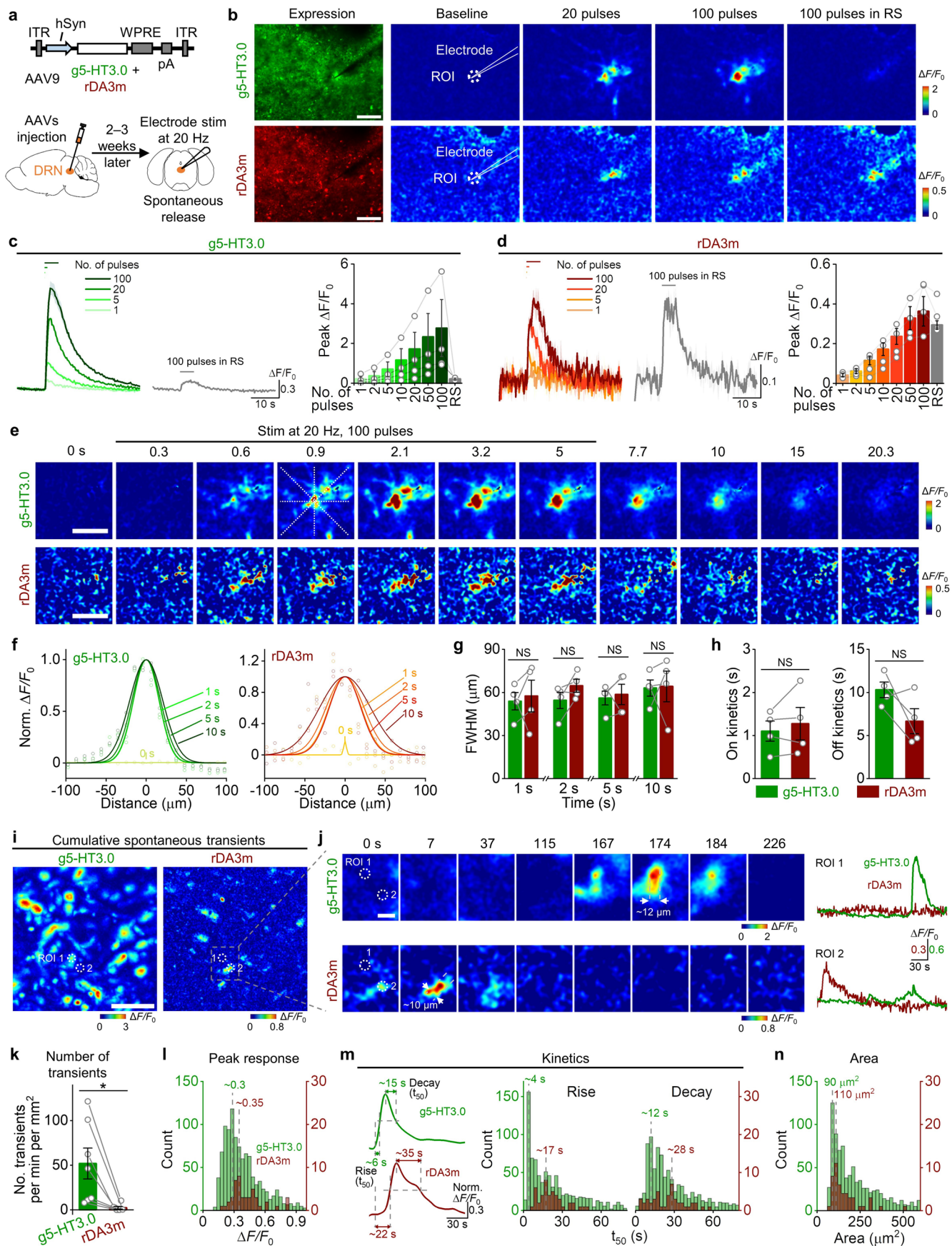
Extended Data Fig. 5 | See next page for caption.

Extended Data Fig. 5 | Dual-color imaging of 5-HT and DA dynamics in acute mouse brain slices with high spatial-temporal resolution. a, Schematic illustrates the mouse brain slice experiments. **b**–**h**, Electrical stimulation evoked 5-HT and DA release. **b**, Representative fluorescence and pseudocolor images of g5-HT3.0 (top) and rDA3m (bottom) at baseline and in response to the indicated electrical stimuli, in the presence of artificial cerebrospinal fluid (ACSF) or 100 μM RS. Similar results were observed for 4 slices. The white dashed circle (50 μm in diameter) indicates the ROI used for further analysis; the white line indicates the stimulating electrode location. Scale bar, 100 μm. **c**–**d**, Representative traces and summary data for changes in g5-HT3.0 (**c**) and rDA3m (**d**) fluorescence in response to the indicated stimuli in ACSF or RS. **e**, Example time-lapse pseudocolor images of g5-HT3.0 (top) and rDA3m (bottom) in response to indicated electrical stimuli. Similar results were observed for 4 slices. The dashed lines were used to analyze spatial and temporal dynamics; image averaged from three trials conducted in one slice. Scale bar, 100 μm. **f**, Example spatial dynamics of the fluorescence changes shown in (**e**). **g**, Summary of the full width at half maximum (FWHM) of activity-dependent

5-HT and DA signals measured in **f** at the indicated time points. Two-tailed paired *t*-tests, $P = 0.7559, 0.1318, 0.741$ and 0.9301 for 1 s, 2 s, 5 s and 10 s, respectively. **h**, Group summary of on and off kinetics for the 100-pulse evoked response of g5-HT3.0 and rDA3m. Two-tailed paired *t*-tests, $P = 0.4308$ and 0.1415 for on and off kinetics, respectively. **i**–**n**, Spontaneous 5-HT and DA release. **i**, Representative pseudocolor images of the cumulative spontaneous transients during a 10-min recording. Similar results were observed for 7 slices. Scale bar, 100 μm. **j**, Representative time-lapse pseudocolor images, and $\Delta F/F_0$ traces of ROIs (10 μm in diameter) from the area indicated by the gray dashed rectangle in **i**. Scale bar, 20 μm. **k**, Number of transients in g5-HT3.0 and rDA3m fluorescence. Two-tailed paired *t*-tests, $P = 0.0226$. **l**, Distribution of the peak response of individual events. **m**, Example traces showing the rise and decay kinetics (t_{50}) of g5-HT3.0 and rDA3m (left), and the distribution of individual events (right). **n**, Distribution of the area of individual events. $n = 4$ slices from 3 mice in **c**,**d**,**g**,**h**; $n = 7$ slices of 3 mice in **k**; $n = 1060$ and 47 events for g5-HT3.0 and rDA3m, respectively, from 7 slices of 3 mice in **l**–**n**. Data are shown as mean ± s.e.m. in **c**,**d**,**g**,**h**,**k**, with the error bars or shaded regions indicating the s.e.m. *$P < 0.05$, n.s., not significant.
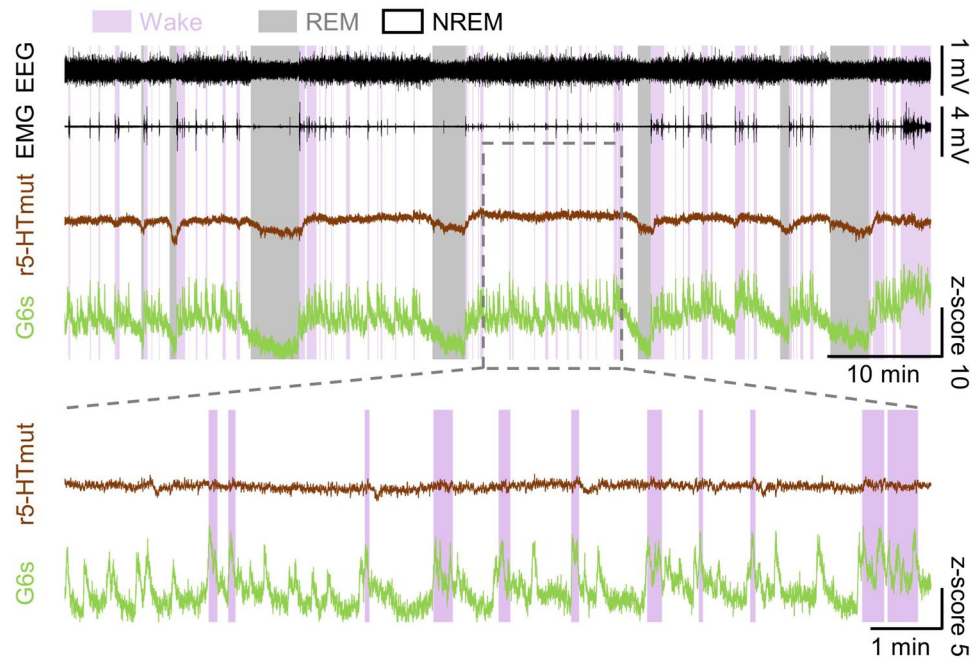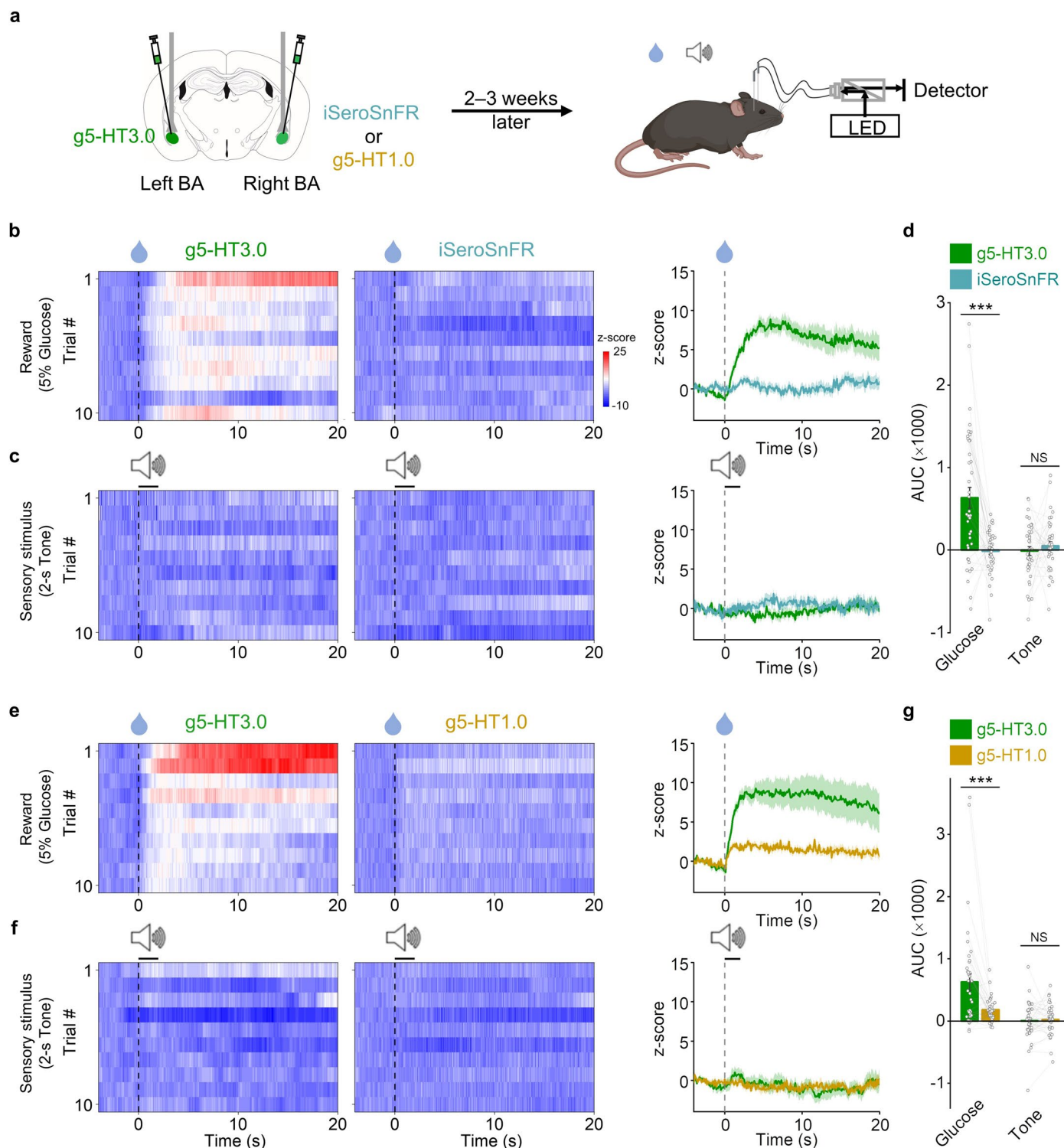
Extended Data Fig. 6 | Representative r5-HTmut and GCaMP6s signals during the sleep-wake cycle in freely moving mice. Representative r5-HTmut and GCaMP6s (G6s) traces in the mouse basal forebrain (BF) along with EEG and EMG recording during the spontaneous sleep-wake cycle.
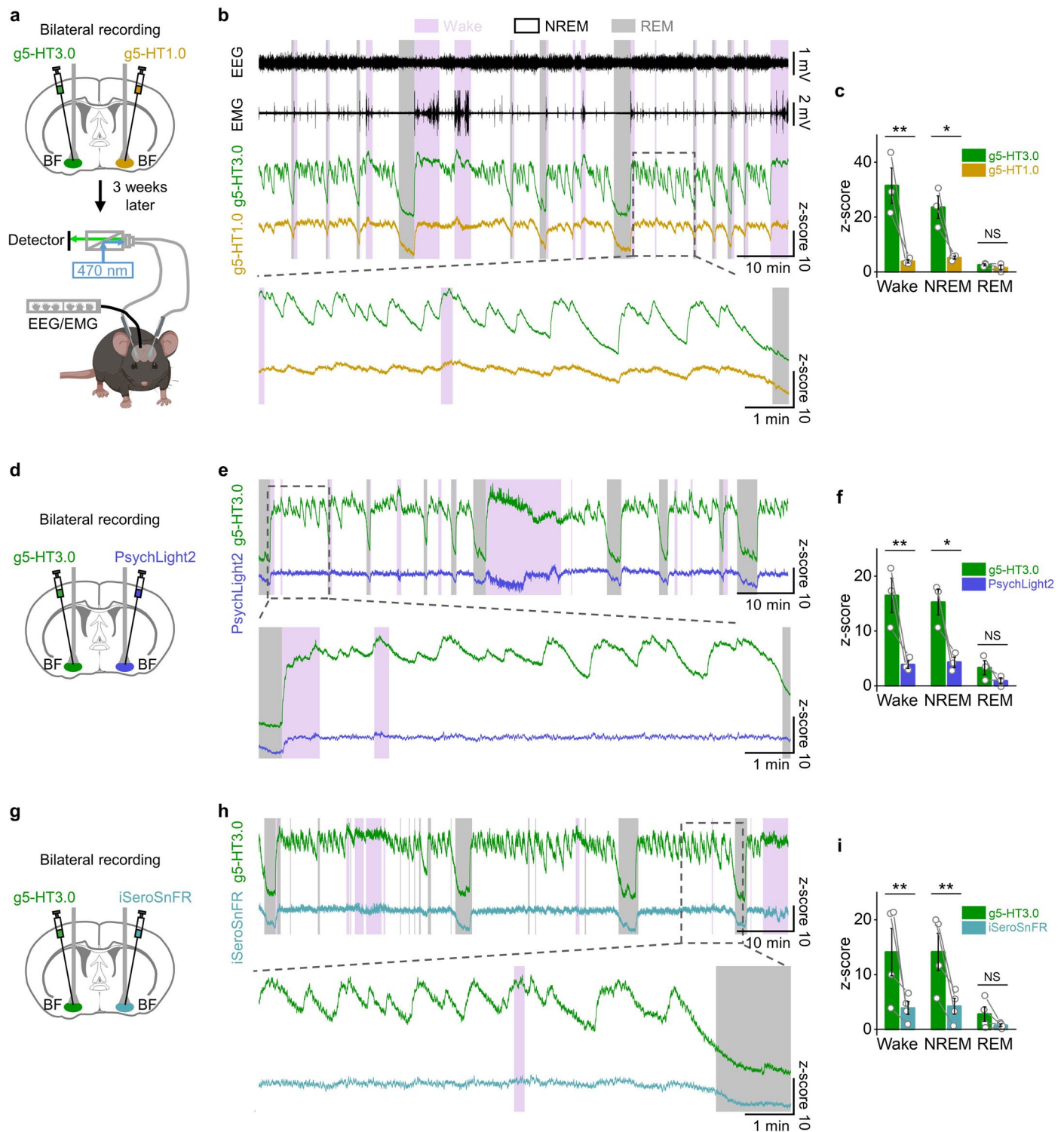
Extended Data Fig. 7 | Comparison of gGRAB$_{5-HT3.0}$ and other green 5-HT sensors during the sleep-wake cycle in freely moving mice. a, Schematic showing the setup of bilateral fiber-photometry recording of g5-HT3.0 and g5-HT1.0 during sleep-wake cycles in mice. **b**, Representative traces of simultaneous EEG, EMG, g5-HT3.0 and g5-HT1.0 recording during sleep-wake cycles in freely behaving mice. Pink shading, wake state; gray shading, REM sleep. **c**, Summary of averaged g5-HT3.0 and g5-HT1.0 signals in indicated sleep-wake states. $n = 3$ mice. Two-way repeated measures ANOVA followed by Tukey's multiple-comparison tests, $P = 0.0034$, 0.014 and 0.83 during wake, NREM and

REM sleep state, respectively. **d–f**, Similar to **a–c**, except bilateral recording of g5-HT3.0 and PsychLight2, $n = 3$ mice in **f**. Two-way repeated measures ANOVA followed by Tukey's multiple-comparison tests, $P = 0.0066$, 0.011 and 0.38 during wake, NREM and REM sleep state, respectively. **g–i**, Similar to **a–c**, except bilateral recording of g5-HT3.0 and iSeroSnFR, $n = 4$ mice in **i**. Two-way repeated measures ANOVA followed by Tukey's multiple-comparison tests, $P = 0.0086$, 0.0095 and 0.47 during wake, NREM and REM sleep state, respectively. Data are shown as mean ± s.e.m. in **c,f,i**, with the error bars indicating the s.e.m. *$P < 0.05$, **$P < 0.01$, n.s., not significant.

Extended Data Fig. 8 | Comparison of gGRAB$_{5-HT3.0}$ and other green 5-HT sensors during reward and tone delivery. a, Schematic illustrates the experimental design. **b**–**c**, Representative pseudocolor images (left) and averaged traces (right) of fluorescence signals (z-score) from g5-HT3.0 and iSeroSnFR in a mouse exposed to 5% glucose (**b**) or 2-s tone (**c**) conditions. The dashed line indicates the delivery of water or tone. **d**, Group analysis of the area under the curve (AUC) of fluorescence signals from g5-HT3.0 and iSeroSnFR in response to the application of 5% glucose or 2-s tone conditions. Two-tailed

paired *t*-tests, $P = 2.4 \times 10^{-5}$ and 0.46 for glucose and tone, respectively. **e**–**g**, Representative pseudocolor images (left), averaged traces (right) and AUC group data (**g**) of fluorescence signals from g5-HT3.0 and g5-HT1.0 during exposure to 5% glucose (**e**) or 2-s (**f**) tone conditions, similar to panels **b**–**d**. Two-tailed paired *t*-tests in **g**, $P = 4.4 \times 10^{-4}$ and 0.632 for glucose and tone, respectively. $n = 40$ trials from 4 mice for each group. Data are shown as mean ± s.e.m. in **b**–**g**, with the error bars or shaded regions indicating the s.e.m. ***$P < 0.001$, n.s., not significant.
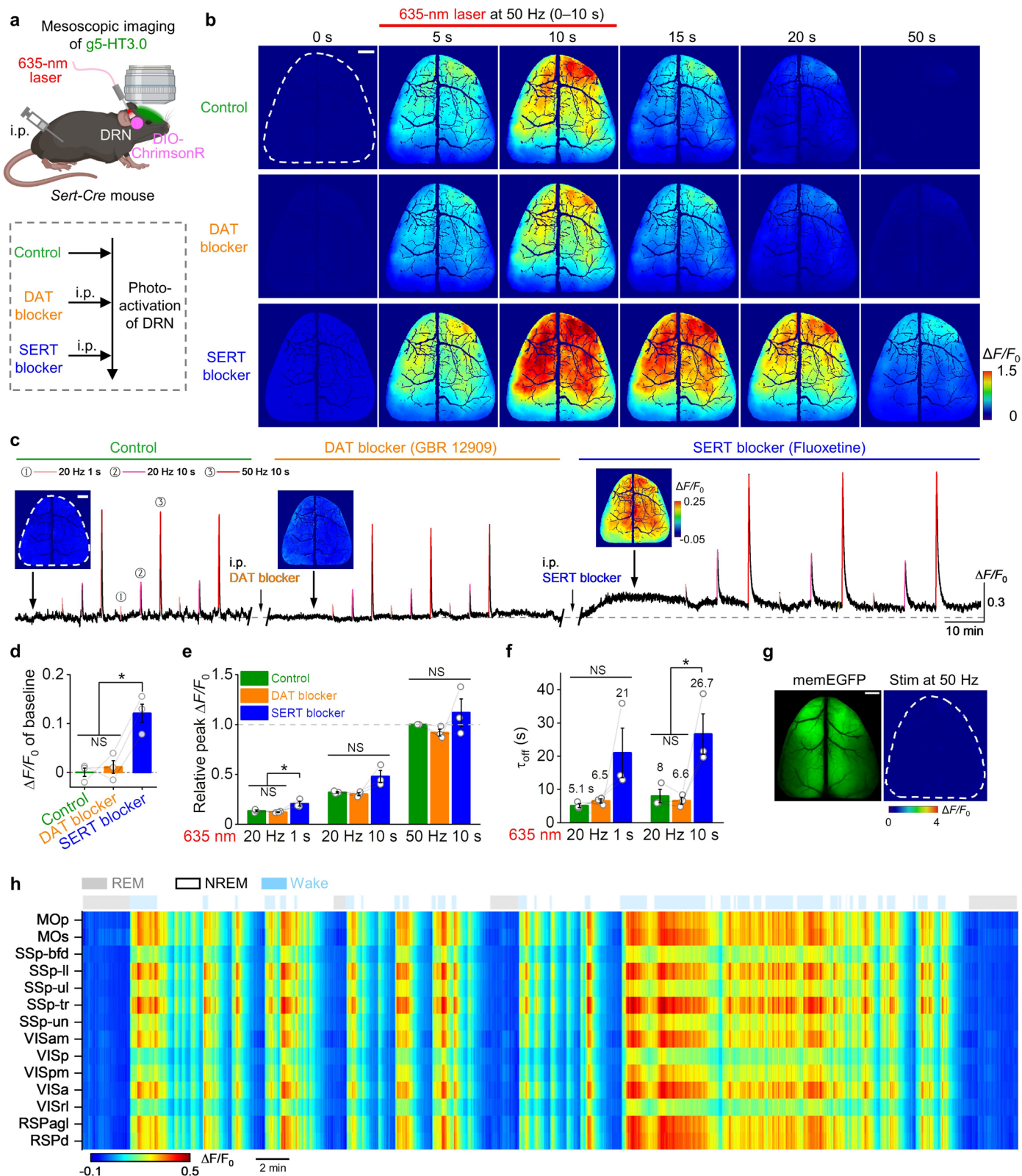
Extended Data Fig. 9 | See next page for caption.

Extended Data Fig. 9 | gGRAB$_{5-HT3.0}$ reveals 5-HT dynamics in mouse dorsal cortex *in vivo*. a, Schematic depicting the protocol for mesoscopic imaging along with optogenetic activation of DRN with different drug treatments. **b**, Representative pseudocolor images in response to the 50 Hz 10 s optical stimulation of DRN with indicated treatments. Scale bar, 1 mm. **c**, Representative trace of g5-HT3.0 with indicated treatments, including the application of different drugs and activation of DRN using a 635-nm laser with different frequencies and durations. Insets above the trace are averaged images in the indicated baseline of different stages. Scale bar, 1 mm. **d**, Group data of averaged g5-HT3.0 baseline fluorescence changes under indicated treatments. $n = 3$ mice. One-way repeated measures ANOVA followed by Tukey's multiple-comparison tests, $F = 19.9$, $P = 0.047$, post hoc test: $P = 0.896$ for control versus DAT blocker, 0.016 for SERT blocker versus control and 0.022 for SERT blocker versus DAT blocker. **e**–**f**, Group summary of optical stimulation evoked peak response (**e**) and decay kinetics (**f**). $n = 3$ mice. One-way repeated measures ANOVA followed by Tukey's multiple-comparison tests. For relative peak $\Delta F/F_0$ in **e**, under 20 Hz 1 s stimulation, $F = 11.1$, $P = 0.023$, post hoc test: $P = 0.81$ for control versus DAT blocker, 0.043 for SERT blocker versus control and 0.026 for SERT blocker versus DAT blocker; under 20 Hz 10 s stimulation, $F = 6.67$, $P = 0.053$; under 50 Hz 10 s stimulation, $F = 1.39$, $P = 0.348$. For decay kinetics τ_{off} in **f**, under 20 Hz 1 s stimulation, $F = 4.06$, $P = 0.182$; under 20 Hz 10 s stimulation, $F = 16.78$, $P = 0.011$, post hoc test: $P = 0.932$ for control versus DAT blocker, 0.018 for SERT blocker versus control and 0.014 for SERT blocker versus DAT blocker. **g**, Representative images showing the memEGFP expression and response to the 50 Hz 10 s optical activation. Scale bar, 1 mm. **h**, Representative heatmap showing changes of g5-HT3.0 fluorescence in different brain regions during sleep-wake cycles. Gray shading, REM sleep; light blue shading, wake state. The dashed white outlines in **b**,**c**,**g** indicate the ROI. Data are shown as mean ± s.e.m. in **d**–**f**, with the error bars indicating the s.e.m. *$P < 0.05$, n.s., not significant.
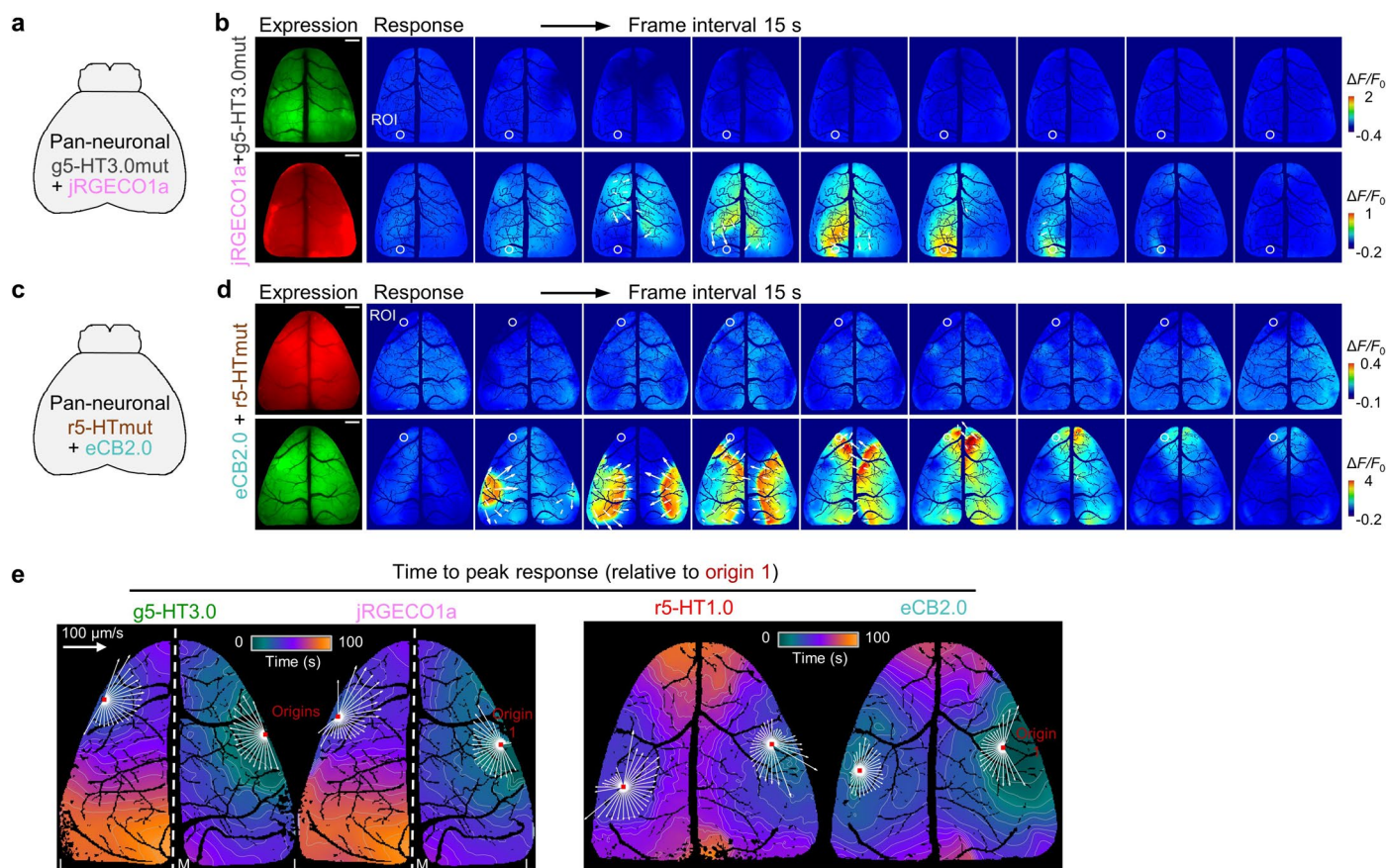
Extended Data Fig. 10 | Mesoscopic imaging of 5-HT, Ca²⁺ and eCB waves during seizures. a, Schematic showing the co-expression of g5-HT3.0mut and jRGECO1a in the mouse dorsal cortex. **b**, Representative images show fluorescence changes of g5-HT3.0mut (top) and jRGECO1a (bottom) during seizures. A ROI labeled with the white circle (500 μm in diameter) shows the maximum response regions of jRGECO1a, which corresponds to the trace in Fig. 5c. White arrows indicate the direction of wave propagation and the length of arrows indicates relative magnitudes of velocities. Scale bar, 1 mm.

c–d, Similar to **a–b**, but co-expressing r5-HTmut and eCB2.0. The ROI shows the maximum response region of eCB2.0 and corresponds to the trace in Fig. 5e. **e**, Representative time to peak response maps of waves relative to the origin 1, monitored by different sensors. Red dots indicate origin locations of waves; white arrows indicate velocity vectors calculated based on the propagation distance and duration along the corresponding direction; L, lateral, M, medial; scale bar of speed, 100 μm/s.

nature portfolio

Corresponding author(s): Yulong Li

Last updated by author(s): Dec 5, 2023

Reporting Summary

Nature Portfolio wishes to improve the reproducibility of the work that we publish. This form provides structure for consistency and transparency in reporting. For further information on Nature Portfolio policies, see our Editorial Policies and the Editorial Policy Checklist.

Statistics

For all statistical analyses, confirm that the following items are present in the figure legend, table legend, main text, or Methods section.

n/a	Confirmed	
☐	☒	The exact sample size (*n*) for each experimental group/condition, given as a discrete number and unit of measurement
☐	☒	A statement on whether measurements were taken from distinct samples or whether the same sample was measured repeatedly
☐	☒	The statistical test(s) used AND whether they are one- or two-sided *Only common tests should be described solely by name; describe more complex techniques in the Methods section.*
☒	☐	A description of all covariates tested
☐	☒	A description of any assumptions or corrections, such as tests of normality and adjustment for multiple comparisons
☐	☒	A full description of the statistical parameters including central tendency (e.g. means) or other basic estimates (e.g. regression coefficient) AND variation (e.g. standard deviation) or associated estimates of uncertainty (e.g. confidence intervals)
☐	☒	For null hypothesis testing, the test statistic (e.g. *F*, *t*, *r*) with confidence intervals, effect sizes, degrees of freedom and *P* value noted *Give P values as exact values whenever suitable.*
☒	☐	For Bayesian analysis, information on the choice of priors and Markov chain Monte Carlo settings
☒	☐	For hierarchical and complex designs, identification of the appropriate level for tests and full reporting of outcomes
☒	☐	Estimates of effect sizes (e.g. Cohen's *d*, Pearson's *r*), indicating how they were calculated

Our web collection on statistics for biologists contains articles on many of the points above.

Software and code

Policy information about availability of computer code

Data collection	1. The NIS-Element 4.51.00 software of Ti-E A1 confocal microscope (Nikon) 2. The Prairie View 5.5 software of Ultima Investigator 2-photon microscope (Bruker) 3. The Harmony 4.9 software of Opera Phenix high-content screening system (PerkinElmer) 4. The commercial software of VICTOR X5 multilabel plate reader (PerkinElmer) 5. The commercial software of the fiber-photometry system (Inper, China) 6. The Spike2 Ver.8.18 software program (Cambridge Electronic Design) 7. Micro-Manager 2.0 (NIH) 8. Arduino 1.8.12 9. The ZEN 2012 (Ver. 11.0.4.190) software of LSM710 confocal microscope (Zeiss)
Data analysis	1. ImageJ 1.53c (NIH) 2. MATLAB R2020b (MathWorks) 3. OriginPro 2020b (Originlab) 4. Adobe Illustrator CC 2018 5. AccuSleep, 04/09/2020 updated, https://github.com/zekebarger/AccuSleep 6. Astrocyte Quantitative Analysis (AQuA), 7/04/2023 updated, https://github.com/yu-lab-vt/AQuA 7. Smart 3.0 (Panlab)

For manuscripts utilizing custom algorithms or software that are central to the research but not yet described in published literature, software must be made available to editors and reviewers. We strongly encourage code deposition in a community repository (e.g. GitHub). See the Nature Portfolio guidelines for submitting code & software for further information.

Data

All manuscripts must include a data availability statement. This statement should provide the following information, where applicable:
- Accession codes, unique identifiers, or web links for publicly available datasets
- A description of any restrictions on data availability
- For clinical datasets or third party data, please ensure that the statement adheres to our policy

The plasmids used to express the sensors in this study and the related sequences are available from Addgene (catalog nos. 208709–208727; https://www.addgene.org/Yulong_Li/). Source data are provided with this paper. The custom-written codes are available under an MIT license from https://github.com/yulonglilab. The human GPCR cDNA library was obtained from the hORFeome database 8.1 (http://horfdb.dfci.harvard.edu/index.php?page=home).

Human research participants

Reporting on sex and gender	N/A
Population characteristics	N/A
Recruitment	N/A
Ethics oversight	N/A

Note that full information on the approval of the study protocol must also be provided in the manuscript.

Field-specific reporting

Please select the one below that is the best fit for your research. If you are not sure, read the appropriate sections before making your selection.

☒ Life sciences   ☐ Behavioural & social sciences   ☐ Ecological, evolutionary & environmental sciences

For a reference copy of the document with all sections, see nature.com/documents/nr-reporting-summary-flat.pdf

Life sciences study design

All studies must disclose on these points even when the disclosure is negative.

Sample size	No statistical methods were used to predetermine sample size. Sample size are indicated for each experiment and were similar to the literatures in the field. [1] Jing, Miao, et al. "A genetically encoded fluorescent acetylcholine indicator for in vitro and in vivo studies." Nature biotechnology 36.8 (2018): 726–737. [2] Sun, F., Zeng, J., Jing, M., Zhou, J., Feng, J., Owen, S. F., ... & Li, Y. (2018). "A genetically encoded fluorescent sensor enables rapid and specific detection of dopamine in flies, fish, and mice." Cell, 174(2), 481–496. [3] Patriarchi, Tommaso, et al. "Ultrafast neuronal imaging of dopamine dynamics with designed genetically encoded sensors." Science 360.6396 (2018). [4] Feng, Jiesi, et al. "A genetically encoded fluorescent sensor for rapid and specific in vivo detection of norepinephrine." Neuron 102.4 (2019): 745–761. [5] Wan, Jinxia, et al. "A genetically encoded sensor for measuring serotonin dynamics." Nature Neuroscience 24.5 (2021): 746–752.
Data exclusions	No data was excluded from the analysis.
Replication	Each experiment in this manuscript is reliably reproducible. The replication number of each result is indicated in the legend of corresponding figures.
Randomization	Animals or cells were randomly assigned into experimental or control groups.
Blinding	The investigators were blinded to group allocation during data collection of behavioral tests in Extended Data Fig. 4c–f. But the investigator were not blinded to other data, since the experimental conditions were obvious to the researchers and the analyses were performed objectively and not subjective to human bias.

Reporting for specific materials, systems and methods

We require information from authors about some types of materials, experimental systems and methods used in many studies. Here, indicate whether each material, system or method listed is relevant to your study. If you are not sure if a list item applies to your research, read the appropriate section before selecting a response.

Materials & experimental systems

n/a	Involved in the study
☒ ☐	Antibodies
☐ ☒	Eukaryotic cell lines
☒ ☐	Palaeontology and archaeology
☐ ☒	Animals and other organisms
☒ ☐	Clinical data
☒ ☐	Dual use research of concern

Methods

n/a	Involved in the study
☒ ☐	ChIP-seq
☒ ☐	Flow cytometry
☒ ☐	MRI-based neuroimaging

Eukaryotic cell lines

Policy information about cell lines and Sex and Gender in Research

Cell line source(s)	HEK293T were purchased from ATCC (cat number CRL-3216). HTLA cells (HEK293 cells stably expressing a tTA-dependent luciferase reporter and β-arrestin2-TEV fusion construct) were a gift from Bryan L. Roth (University of North Carolina Chapel Hill).
Authentication	The cell lines were authenticated based on the morphology under microscope and the analysis of the growth curve.
Mycoplasma contamination	No mycoplasma contamination.
Commonly misidentified lines (See ICLAC register)	No commonly misidentified cell lines were used.

Animals and other research organisms

Policy information about studies involving animals; ARRIVE guidelines recommended for reporting animal research, and Sex and Gender in Research

Laboratory animals	For cultured cortical neurons, both male and female postnatal day 0 (P0) Sprague-Dawley rats were used. For fiber photometry recording experiments, either adult wild-type C57BL/6J (Beijing Vital River laboratory) or Sert-Cre (The Jackson Laboratory) mice were used. For mesoscopic imaging experiments, either P0–P1 wild-type C57BL/6J (Beijing Vital River laboratory) or Sert-Cre mice were injected with AAVs, and were used for surgery and imaging after eight weeks. For behavior assays and acute mouse brain slice experiments, adult wild-type C57BL/6J mice (6–8 weeks of age) were used. All mice were group-housed or pair-housed in a temperature (18–23 °C), humidity (40–60%) and light/dark cycle (12-h/12-h) controlled room, with food and water available ad libitum.
Wild animals	No wild animals were used in the study.
Reporting on sex	Both male and female mice were randomly selected and used in the study.
Field-collected samples	No field-collected samples were used in the study.
Ethics oversight	All procedures for animal surgery and maintenance were performed using protocols that were approved by the Animal Care & Use Committees at Peking University.

Note that full information on the approval of the study protocol must also be provided in the manuscript.